Fault-valve instability: A mechanism for slow slip events

So Ozawa^{1,2}, Yuyun Yang³, Eric M. Dunham^{1,4}

¹Department of Geophysics, Stanford University
²Earthquake Research Institute, University of Tokyo
³Earth and Environmental Sciences Programme, The Chinese University of Hong Kong
⁴Institute for Computational and Mathematical Engineering, Stanford University

Key Points:

11

13

- We analyze the dynamics of fault slip with fault-zone fluid flow and fault-parallel permeability enhancement with slip and sealing with time
- Fault-valve instability produces unidirectional aseismic slip and pore pressure pulses even with velocity-strengthening friction
- Subduction zone earthquake cycle simulations show that the fault-valve instability can produce slow slip events below the seismogenic zone

Corresponding author: So Ozawa, sozawa@stanford.edu

Abstract

15

16

17

19

20

21

22

23

24

25

27

28

29

30

31

32

33

35

37

38

39

40

42

43

44

46

47

49

50

51

52

53

54

55

56

57

58

62

63

Geophysical and geological studies provide evidence for cyclic changes in fault-zone pore fluid pressure that synchronize with or at least modulate slip events. A hypothesized explanation is fault valving arising from temporal changes in fault zone permeability. In our study, we investigate how the coupled dynamics of rate and state friction, along-fault fluid flow, and permeability evolution can produce slow slip events. Permeability decreases with time, and increases with slip. Linear stability analysis shows that steady slip with constant fluid flow along the fault zone is unstable to perturbations, even for velocitystrengthening friction with no state evolution, if the background flow is sufficiently high. We refer to this instability as the "fault valve instability." The propagation speed of the fluid pressure and slip pulse, which scales with permeability enhancement, can be much higher than expected from linear pressure diffusion. Two-dimensional simulations with spatially uniform properties show that the fault valve instability develops into slow slip events, in the form of aseismic slip pulses that propagate in the direction of fluid flow. We also perform earthquake sequence simulations on a megathrust fault, taking into account depth-dependent frictional and hydrological properties. The simulations produce quasi-periodic slow slip events from the fault valve instability below the seismogenic zone. in both velocity-weakening and velocity-strengthening regions, for a wide range of effective normal stresses. A separation of slow slip events from the seismogenic zone, which is observed in some subduction zones, is reproduced when assuming a fluid sink around the mantle wedge corner.

Plain Language Summary

Slow slip events are observed in subduction zones worldwide. Their mechanism is not well understood, but geophysical and geological research suggests a relation with recurring changes in fluid pressure within the fault zone. Here we explore the fault valve mechanism for slow slip events using mathematical and computational models that couple fluid flow through fault zones with frictional slip on faults. The fault valve mechanism (arising from cyclic changes in the permeability or resistance to fluid flow) produces pulses of high fluid pressure, accompanied by slow slip, that advance along the fault in the direction of fluid flow. We quantify the conditions under which this occurs as well as observable properties like the propagation speed and rate of occurrence of slow slip events. We also perform simulations of subduction zone slow slip events using fault zone and frictional properties that vary with depth in a realistic manner. The simulations show that the fault valve mechanism can produce slow slip events with approximately the observed rate of occurrence, while also highlighting some discrepancies with observations that must be addressed in future work.

1 Introduction

Tectonic faults slip both seismically and aseismically. In this century, we have become increasingly confident that aseismic slip is a ubiquitous phenomenon worldwide, especially along subduction megathrusts (Nishikawa et al., 2019; Bürgmann, 2018). Slow slip events (or, more generally, slow earthquakes) have much slower slip rates than ordinary earthquakes, but what limits their slip rate remains unclear. What determines the spatial distribution of fast and slow earthquakes is also an open question. Our work aims to address both of these questions, using a model for slow slip events that couples fault zone fluid flow, permeability evolution, and slip. Our work builds on the modeling study of Zhu et al. (2020) that showed how this coupling can produce periodic slow slip events. However, that study was limited to a few simulations and speculation about the feedback mechanisms producing the slow slip events. Here we combine linear stability analysis and nonlinear simulations to understand the role of each process and quantify properties such as the growth rate and phase velocity of unstable modes that help

explain the recurrence interval and propagation speed of the slow slip events. Below we provide a brief review of several proposed mechanisms for slow slip events, highlighting in particular the role of fluids and explaining how our work fits into this broader context.

The recurrent nature of slow slip events is easily explained by the concept of stickslip. Shear stress accumulates within a locked region, then is relaxed by a reduction in the frictional shear strength of the fault. Because frictional strength is the product of friction coefficient and effective normal stress (total normal stress minus pore fluid pressure), that strength reduction can occur by a drop in friction coefficient or an increase in fluid pressure.

1.1 Slow slip from changes in friction coefficient

65

66

67

70

71

72 73

74

75

76

77

79

80

81

82

83

87

88

89

92

93

95

100

101

102

103

104

105

106

107

108

109

111

112

113

114

Rate and state friction laws are widely used to explain stick-slip behavior through changes in the friction coefficient (Dieterich, 1979; Marone, 1998; Tse & Rice, 1986; Scholz, 1998). For constant effective normal stress, steady slip is always stable for a velocity-strengthening fault and is conditionally unstable for a velocity-weakening fault (Ruina, 1983; Rice et al., 2001) (Figure 1a). Slow slip occurs on a velocity-weakening fault when the fault length is near the critical wavelength for instability or nucleation length (Liu & Rice, 2007). We refer to this as the neutral stability model. In other words, the acceleration of slip that accompanies nucleation is stalled by elastic interactions with the surrounded locked or aseismically creeping portions of the fault, preventing the instability from becoming a fast rupture. The main criticism of this model is that the parameter range of slow slip occurrence is very narrow (Rubin, 2008), especially when the slip law is used for state evolution.

The nucleation length in rate and state friction is inversely proportional to effective normal stress, so high fluid pressure leads to conditions more favorable for slow slip events. High fluid pressure at the source regions of slow slip is suggested by several observations (Peacock et al., 2011; C. Condit & French, 2022; Kodaira et al., 2004), although the actual value of effective stress is not well constrained. The high Vp to Vs ratio obtained from seismic tomography at source regions of slow slip is consistent with high fluid pressure in laboratory experiments (Peacock et al., 2011), although a more recent study suggests that the relationship between fluids and Vp to Vs ratio is not so simple (Brantut & David, 2019). Furthermore, the tidal sensitivity of low-frequency earthquakes (Thomas et al., 2012) requires very low effective normal stress, at least for standard choices of frictional parameter values. We also note that nucleation length depends inversely on the rate and state velocity-dependence parameter a-b, so extremely low effective normal stress might not be required if a-b is very small (i.e., if the fault is close to velocity neutral). Finally, the low stress drop ($\sim 10 \text{ kPa}$) of slow slip events (Gao et al., 2012) has also been interpreted as evidence for low effective normal stress, though again this might not be required if a - b is small (or if slow slip events arise from some other process).

Several processes have been invoked to expand the range of frictional and effective stress conditions producing slow slip. These include heterogeneous frictional properties and geometrical complexity (Nie & Barbot, 2021; Skarbek et al., 2012; Romanet et al., 2018; S. W. Ozawa et al., 2019) and dilatant strengthening, referring to a reduction in pore fluid pressure and increase in frictional strength caused by inelastic porosity increase with slip (Segall et al., 2010; Liu & Rubin, 2010). This line of work has recently been expanded to use microphysically-based friction and porosity evolution laws (Chen, 2023) and to consider the effects of creep compaction (Yang & Dunham, 2023) and interactions with viscous flow in ductile fault roots (Perfettini & Molinari, 2023).

Slow slip can also occur if friction transitions from velocity weakening to velocity strengthening friction at a slip velocity that is well below that required for inertial effects to become important (Shibazaki & Iio, 2003; Kato, 2003; Matsuzawa et al., 2013;

Hawthorne & Rubin, 2013; Im et al., 2020). The acceleration of slip is limited due to the increase in frictional resistance when slip velocity exceeds the threshold for the transition to velocity strengthening behavior, which allows slow propagation of the rupture. There is both experimental evidence and theoretical justification for this transition (Nakatani & Scholz, 2006; Chen et al., 2017; Shimamoto, 1986; Shreedharan et al., 2022; Okuda, Kitamura, et al., 2023; Bar-Sinai et al., 2014; Barbot, 2023; Mei & Wang, 2024). A possible criticism is that this frictional behavior is observed in experiments over a much broader range of pressure, temperature, and lithologic conditions than those characterizing the source region of slow slip events.

1.2 Slow slip from changes in pore pressure

The mechanisms described thus far all require velocity-weakening friction and a reduction in friction coefficient to cause slow slip. Alternative mechanisms for slow slip appeal to weakening by increases in fluid pressure. These can be caused by thermal pressurization (Segall & Rice, 2006; Garagash, 2012), poroelastic bimaterial effects (Heimisson et al., 2019), and inelastic compaction (Dal Zilio & Gerya, 2022). In these studies, the changes in fluid pressure and fluid flow are localized around the slipping portion of the fault and along-fault fluid flow is neglected or at least unimportant in the instability mechanism. Other studies, reviewed subsequently, examine the effects of along-fault fluid flow and its role in producing slow slip events.

In subduction zones, fluids are sourced at shallow depths by compaction of sediments and the dehydration of clays and other minerals (Saffer & Tobin, 2011) and at greater depths by dehydration from metamorphic and metasomatic reactions (Van Keken et al., 2011; Tarling et al., 2019; C. B. Condit et al., 2020). Fluids can also ascend from the mantle (Nishiyama et al., 2020; Cordell et al., 2023). There is much evidence that fluid ascent occurs in an unsteady manner involving cyclic changes in fluid pressure. For example, Warren-Smith et al. (2019) interpret temporal changes in the focal mechanisms of earthquakes in the subducting oceanic slab around slow slip events as evidence for pressurization prior to and depressurization following slow slip events. Similarly, a $\sim 0.1 \text{ km/s}$ increase in S-wave velocity near the top of the subducting slab following slow slip events is interpreted to be caused by depressurization from fluid release (Gosselin et al., 2020). Gravity changes have also been explained by fluid migration during slow slip events (Tanaka et al., 2018). Exhumed outcrops provide geologic evidence for cyclic pressure and permeability changes in the form of crack-seal textures observed in veins and the variable orientation of extensional and shear veins (Ujiie et al., 2018; Otsubo et al., 2020; C. Condit & French, 2022).

The fault valve model of Sibson (1992) is commonly invoked to explain the cyclic variation of pore fluid pressure. In this model, the fault zone permeability is low between slip events, so that fluid overpressure develops in response to continued fluid influx from depth. Once the fault slips, in part due to the weakening caused by fluid overpressure, permeability increases as a result of the dilation of fault gouge and the generation of microfractures. This allows upward flow that at least partially relieves the overpressure. After the fault slips, the permeability decreases, which again leads to fluid overpressure development. This process, in addition to the accumulation and release of shear stress, controls the periodicity of slip events.

Fault valving requires permeability evolution, for which there is ample evidence (Saffer, 2012; Ingebritsen & Manning, 2010). Shallow (<1 km depth) injection experiments show an order of magnitude or more of permeability increase caused by assismic slip (Bhattacharya & Viesca, 2019; Cappa, Guglielmi, Nussbaum, et al., 2022). Permeability increases with slip are also seen in some laboratory experiments (Im et al., 2019; Ye & Ghassemi, 2018). Fault valving also requires permeability reduction between slip events. Laboratory experiments, borehole measurements following earthquakes, and theory provide evidence

for permeability decreases during the interseismic period due to closure of fractures by high normal stress and precipitation of minerals from fluid (Giger et al., 2007; Yehya & Rice, 2020; Xue et al., 2013; Saishu et al., 2017; Fisher et al., 2019), although a recent study argues that the precipitation of silica might be too slow to explain the sealing over the time scale of slow slip events (Williams & Fagereng, 2022).

Models exploring the connection between fault valving and slow slip events or tectonic tremor have recently been developed. Some of these focus exclusively on fluid pressure evolution (Cruz-Atienza et al., 2018) or assume a one-way coupling from imposed fluid pressure changes to fault slip (Perez-Silva et al., 2023). Zhu et al. (2020) utilized a two-way coupling between fluid pressure and slip, with steady fluid influx from depth, and showed that permeability evolution as described above can produce periodic pulses of elevated pore pressure and aseismic slip with features similar to slow slip events. Our study continues this line of research with a comprehensive analysis of these events, which we show to be caused by an instability that is fundamentally different from the classical rate and state instability on a velocity weakening fault.

1.3 Fault valve instability

Here, we provide a conceptual explanation of the fault valve instability. Consider steady sliding and constant flow, which is perturbed by a local increase in slip rate. This locally increases the permeability. If background flow is present, the permeability gradients on either side of the perturbation create a fluid flow gradient. The negative flow gradient on the downstream side of the perturbation leads to fluid accumulation and increases the fluid pressure. If the shear stress remains relatively constant, then the friction coefficient also increases. The increase in friction coefficient, for velocity-strengthening faults or simply through the direct effect, increases the slip velocity on the downstream side of the initial slip velocity perturbation. This is a positive feedback that promotes instability growth and propagation in the direction of flow (Figure 1a). However, there are processes which can counteract and even prevent the instability. Slip induces a reduction in shear stress through the elastic response of the solid. The reduction in shear stress acts to decrease slip velocity. Similarly, along-fault pressure diffusion can reduce the destabilizing pressurization. An important contribution of our work is quantifying the conditions for instability and the role of these various processes in promoting or inhibiting the instability.

We also remark that the fault valve instability is a general instability mechanism that most likely occurs for a broad class of permeability evolution laws. Recently, Zhu et al. (2020) introduced a specific, ad hoc permeability evolution law and demonstrated the emergence of swarm-like seismicity and quasi-periodic slow slip events that propagate up-dip (in the direction of fluid flow), using earthquake sequence simulations. In this study, we show that the instability occurs for any permeability evolution law for which permeability evolves with slip or time toward a steady-state permeability that depends on slip rate. The instability also requires either a non-zero direct effect or purely velocity-strengthening friction. As friction switches from velocity-strengthening to velocity-weakening, the fault valve instability transitions into the classical rate-state instability that is driven by frictional weakening. Overall, this work demonstrates the destabilization of steady fault sliding and fluid flow for a sufficiently large background flow rate and permeability enhancement, regardless of the velocity dependence of friction.

1.4 Structure of the paper

The paper is structured as follows. Section 2 introduces the governing equations of our model. In Section 3 we show the emergence of the fault valve instability by using linear stability analysis to study small perturbations about steady sliding and steady fluid flow through a fault zone with spatially uniform properties. Analysis of this most

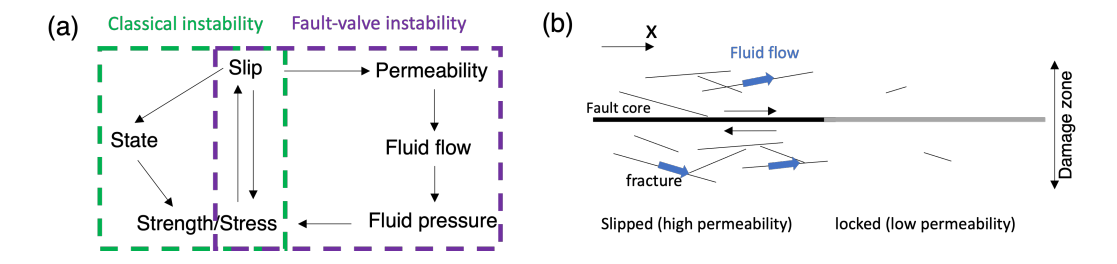


Figure 1. (a) Concepts of both classical and fault-valve instability are shown with the relationship between different variables. (b) Schematic of fault zone structure and fluid flow. The fluid flows through fractures in a fault damage zone that is much wider than the fault core. Permeability is higher in the slipped region than unslipped region.

idealized problem allows us to define the minimal conditions for unstable slip. We also quantify properties of the instability such as growth rate and phase velocity that are shown later to accurately predict the recurrence interval and propagation rate of slow slip events in numerical simulations. Section 4 uses earthquake sequence simulations with spatially uniform properties to validate the linear stability analysis and explore how the fault valve instability develops in the nonlinear regime. With the insight gained from these more idealized setups, we turn in Section 5 to more complex subduction zone earthquake sequence simulations. We account for realistic depth variations in frictional properties, stress conditions, and parameters in the permeability evolution model, with fluid production source terms motivated by the petrologically expected rates and depths of dehydration reactions. In particular, the timescale of permeability reduction decreases with increasing temperature and depth. The simulations show how the fault valve instability produces slow slip events below the seismogenic zone. In the Discussion (section 6), we compare our model with previous work and highlight the limitations as well as opportunities for future work. Section 7 concludes the paper.

2 Governing Equations

217

218

220

221

222

223

224

225

228

229

230

231

232

233

234

235

237

238

239

240

241

242

243

244

245

246

247

249

250

251

2.1 Fluid pressure diffusion

We assume that fluid flow is confined within the fault zone and do not consider faultnormal flow (Figure 1b). This assumption is often justified for three reasons. First, fault damage zones typically have higher permeability and storage compared to the host rock due to the high density of fractures (Wibberley & Shimamoto, 2003; D. A. Lockner et al., 2009; Faulkner et al., 2010). In shallow megathrusts, permeabilities three to six orders of magnitude higher than the host rock are required to explain the geochemical and thermal anomalies observed in seepage and borehole studies (Saffer, 2012). This high contrast is not obvious in the deeper plate boundary shear zone where deep slow slip events occur, but there are several field observations of exhumed subduction zones showing that the plate boundary has higher permeability than the surrounding rock (Bebout & Penniston-Dorland, 2016). Even with a high permeability contrast between the fault zone and the host rock, this assumption is only valid if the time scale of interest (i.e., the duration and recurrence interval of slow slip events) is shorter than the time required for significant depressurization of the fault zone by leakage of fluids into the host rock (Yang & Dunham, 2021). Second, the development of foliated structures with accumulated slip and shearing leads to a significant permeability contrast between fault-parallel and fault-normal directions (Kawano et al., 2011). This will further restrict fault-normal flow. Third, the time scale of interest is longer than the characteristic fault-normal diffusion time within

the highly permeable damage zone, resulting in a uniform fluid pressure across the damage zone.

When flow is confined to the fault zone and fault-normal flow is neglected, the width of the fault zone is constant, and the mechanical response of the matrix is linear elastic, the fluid pressure diffusion equation is

$$\beta \phi \frac{\partial p}{\partial t} = \frac{\partial}{\partial x} \left(\frac{k}{\eta} \frac{\partial p}{\partial x} \right), \tag{1}$$

where β is the sum of the pore and fluid compressibilities, ϕ is the porosity, k is the permeability, and η is the fluid viscosity. The fluid pressure p is interpreted as overpressure (fluid pressure minus hydrostatic pressure) if some component of gravity is present in the direction of x. The values of $\beta\phi$ and k should be interpreted as the average in the fault-normal direction across the width of the damage zone (Yang & Dunham, 2023), which is typically much wider than the thickness of the localized inelastic shear deformation that accommodates slip.

Note that some models make the opposite assumption: retaining fault-normal diffusion and neglecting fault-parallel diffusion (Segall et al., 2010; Rice, 2006). This is appropriate when the fluid pressure gradient is much higher in the fault-normal direction, which occurs when a localized source or sink of fluid pressure associated with dilatancy or thermal pressurization is considered and there is insufficient time for pressure equilibration across the width of the damage zone. Membrane diffusion (Segall et al., 2010; Chen, 2023) is often used to approximate fault-normal diffusion within low permeability fault core surrounded by highly permeable damage zones as observed from exhumed faults (Wibberley & Shimamoto, 2003; D. Lockner et al., 2000). Accounting for both fault-parallel and fault-normal diffusion leads to a more complicated set of equations, and would be an important future extension of our model (see also Heimisson et al. (2022)).

There are well-established relationships between permeability k and porosity ϕ in rock physics (Mavko et al., 2020; Bernabé et al., 2003). In this study we assume that ϕ remains constant (except for its small elastic variations captured in the compressibility β) even though the permeability evolves with time. Our underlying assumption is that changes in permeability result from changes in tortuosity (i.e., pore connectivity) rather than from changes in porosity. If porosity were changing in an inelastic manner, a suction or source term would be added to equation (1). The importance of this additional term would depend on the sensitivity of the permeability to changes in porosity. Similar assumptions were made by Zhu et al. (2020) and Dublanchet and De Barros (2021). It is an important future study to include both inelastic porosity and tortuosity changes to explore more realistic situations and to quantify the relative importance of these two mechanisms for permeability evolution. That said, it seems impossible to explain the order of magnitude or larger changes in permeability that are routinely invoked for fault valving through standard relations between k and ϕ (see discussion in Yang and Dunham (2023)).

Finally, we remark that the specific storage $\beta\phi$ is treated as a constant even though our model accounts for elastic porosity changes (through the pore compressibility that partially determines β). Order of magnitude estimates show that the error associated with this approximation is only a few percent, much smaller than the other nonlinearities that we do account for.

2.2 Permeability evolution

Many experiments reveal that permeability decreases with increasing effective normal stress σ_e (total normal stress minus pore fluid pressure) because of elastic deformation of pores (David et al., 1994). We account for this through a general relation of the

form

$$k = k^* f(\sigma_e), \tag{2}$$

where k^* is a reference permeability. A commonly used parameterization that is consistent with many laboratory experiments is

$$f(\sigma_e) = e^{-\sigma_e/\sigma^*}. (3)$$

The stress sensitivity parameter σ^* is typically of order 10 MPa for fault zone rocks (Mitchell & Faulkner, 2012; Wibberley & Shimamoto, 2003).

Cruz-Atienza et al. (2018) used the same equation with fixed k^* and showed a wave-like solution to the nonlinear pressure diffusion equation, and suggested that the resulting pressure pulse might trigger tremor. In our simulation starting from the steady state, however, the effect of this term is small in comparison to the permeability change from the evolution law for k^* presented below. On the other hand, the value of σ^* is critically important in the steady-state effective normal stress profile in the depth-dependent problem, as shown in Section 5.

Permeability also evolves with slip and time (Im et al., 2019; Zhu & Wong, 1997; Cappa, Guglielmi, & De Barros, 2022; Ishibashi et al., 2018; Giger et al., 2007; Morrow et al., 2001). Although these experiments provide valuable insights, most of them are concerned with permeability of fault gouge or fractures, whereas we are more concerned with permeability evolution in the damage zone. Because of the lack of constraints and to ensure our analysis is broadly applicable, we assume a general form for permeability evolution:

$$\frac{dk^*}{dt} = g(k^*, V). (4)$$

As an example of the permeability evolution law, Zhu et al. (2020) introduced

$$g(k^*, V) = \frac{V}{L}(k_{\text{max}} - k^*) + \frac{1}{T}(k_{\text{min}} - k^*).$$
 (5)

We use this law in our nonlinear earthquake sequence simulations. The first term represents the increase of k^* towards k_{max} by processes such as microfracturing (Figure 1b). The constant L characterizes the slip distance required for the permeability increase. The second term is the exponential decrease with time toward k_{min} over time scale T due to healing and sealing of the microfractures. Some laboratory experiments support the exponential decay of permeability (Giger et al., 2007), but others show a power-law decay (Im et al., 2019). At steady state, k^* is an increasing function of velocity:

$$k_{ss}^*(V) = \frac{k_{\text{max}} + k_{\text{min}}L/TV}{1 + L/TV}.$$
 (6)

From equation (6), $k_{ss}^* \sim k_{\rm max}$ for $T > L/V_0$ and healing is too slow to be effective. We use a very small value for $k_{\rm min}$ so that this value does not affect the result. There are four parameters in equation (5). The healing time T is assumed to be about one year from some observations at about 1 km depth (Xue et al., 2013), but depends on the temperature from laboratory experiments (Giger et al., 2007; Morrow et al., 2001; Tenthorey & Gerald, 2006). The slip distance L is more difficult to constrain, but Im et al. (2019) reports L to be about 1 mm in slide-hold-slide experiments. It is not necessary to be the same as state evolution distance in rate and state friction (see next section) because our permeability is considered to be averaged across the fault damage zone.

2.3 Friction

We use the regularized rate and state friction law, and state evolution is governed by the aging law (Dieterich, 1979; Ruina, 1983), in which

$$\frac{\tau}{\sigma_e} = a \sinh^{-1} \left(\frac{V e^{-\psi/a}}{2V_0} \right),\tag{7}$$

$$\frac{d\psi}{dt} = \frac{b}{d_c} \left(V_0 e^{\frac{f_0 - \psi}{b}} - V \right),\tag{8}$$

where τ is the shear stress, ψ is the state variable, f_0 is the reference friction coefficient, a is the coefficient of the direct effect, b is the coefficient of the evolution effect, and d_c is the characteristic slip distance. This form is used in the numerical simulations. The linearized form of this friction law, which is used in the subsequent linear stability analysis, is generic and applies to any rate and state friction law of the form described by Rice et al. (2001).

3 Linear stability analysis

We investigate the stability of the system in the previous section to small perturbations about steady state. Steady state quantities are denoted with a subscript 0 ($k_0, V_0, q_0, \sigma_0, \tau_0$). Sliding occurs on a planar fault in a homogeneous solid whole-space. The solid response is linear isotropic elastic and we neglect inertia because of our focus on slow slip. The analysis to follow applies equally to antiplane shear and plane strain perturbations, with the elastic modulus μ^* appearing in the relation between shear stress and slip being equal to the shear modulus for antiplane shear and the shear modulus divided by one minus Poisson ratio for plane strain. In this steady state, the fault is sliding at the loading velocity V_0 and the fluid flow rate q_0 is uniform:

$$q_0 = -\frac{k_0}{\eta} \frac{dp_0}{dx}. (9)$$

Without loss of generality, we assume $q_0 > 0$, i.e., fluids flow in the positive x direction in steady state. The unperturbed effective normal stress, σ_0 , is spatially uniform. We perform the linear stability analysis for the general form of the permeability evolution and the rate-and-state friction law.

The permeability evolution law (4) and (5) linearizes about the steady state as (see Appendix)

$$\frac{dk}{dt} = -\frac{k_0}{\sigma^*} \frac{d\sigma_e}{dt} - \frac{1}{T_k} \left[k - k_{ss}^{lin}(V, \sigma_e) \right], \tag{10}$$

$$k_{ss}^{lin}(V, \sigma_e) = k_0 - k_0 \frac{\sigma_e - \sigma_0}{\sigma^*} + \Delta k \frac{V - V_0}{V_0},$$
 (11)

where V is slip velocity, T_k is the time scale for the linearized permeability evolution law, Δk is the characteristic change in permeability, and σ^* is the stress sensitivity parameter characterizing the dependence of permeability on effective normal stress.

The rate and state friction law is also linearized (Rice et al., 2001):

$$\frac{\mathrm{d}\tau}{\mathrm{d}t} = \frac{a\sigma_0}{V_0} \frac{\mathrm{d}V}{\mathrm{d}t} + f_0 \frac{\mathrm{d}\sigma_e}{\mathrm{d}t} - \frac{V_0}{d_c} \left[\tau - \tau_{ss}(\sigma_e, V)\right],\tag{12}$$

$$\tau_{ss}(\sigma_e, V) = \tau_0 + f_0(\sigma_e - \sigma_0) + (a - b)\sigma_0 \frac{V - V_0}{V_0}.$$
 (13)

We choose the reference state to be identical to the steady state. The frictional strength τ changes with fluid pressure p via the effective stress law $\sigma_e = \sigma - p$. Laboratory experiments show that this law does not hold instantaneously, at least for changes in total normal stress (Linker & Dieterich, 1992). After the step in effective normal stress, a finite displacement is required to reach the new steady state shear strength expected from the same friction coefficient.

3.1 Characteristic equation

We seek a solution for $\exp(st + i\kappa x)$ perturbations for complex-valued growth rate s and real-valued wavenumbers κ . The wavelength is $\lambda = 2\pi/\kappa$. We derive the relationship between wavenumber κ and the dimensionless growth rate $S = sT_k$, which is

known as the characteristic equation. Except in special limits, there is more than one solution to the characteristic equation. The system is unstable when the maximum value of Re(s) is positive, and the perturbation grows with time.

Perturbations are studied in the context of Fourier eigenmodes $\exp(i\kappa x)$ because the coefficients of the problem (i.e., frictional and fluid transport properties) are spatially uniform. Furthermore, perturbations having arbitrary spatial dependence can be decomposed into the superposition of Fourier modes. In natural systems, we expect perturbations at all wavelengths smaller than the overall length of the fault. For faults with spatially variable properties, the eigenmodes will have non-Fourier spatial dependence. However, if the properties vary slowly, then the constant coefficient analysis presented here still has relevance when perturbation wavelengths are shorter than the length scale over which properties vary. In section 5, we perform subduction zone simulations with depthvarying properties. We show how results derived in this section from the linear stability analysis help inform the depth extent and other properties of slow slip events occurring via the fault valve instability mechanism.

According to Appendix, the characteristic equation is

$$PS^{2} + \left(\frac{a-b}{a}PJ + 1\right)S + J + iPQ\frac{S(S+J)}{(S+1)(S+R+iM)} = 0,$$
(14)

with five dimensionless parameters defined as follows:

391

393

400

401

403

405

406

409

410

411

412 413

414

415

418

419

420

422

423

426

427

428

429

430

431

432

434

435

436

$$P = \frac{2a\sigma_0}{\mu^*|\kappa|V_0T_k},\tag{15}$$

$$P = \frac{2a\sigma_0}{\mu^* |\kappa| V_0 T_k},$$

$$Q = \frac{\kappa f_0 q_0 \Delta k T_k}{k_0 \beta \phi a \sigma_0},$$

$$R = c_0 \kappa^2 T_k,$$
(15)

$$R = c_0 \kappa^2 T_k, \tag{17}$$

$$M = \frac{\kappa q_0 T_k}{\sigma^* \beta \phi},\tag{18}$$

$$J = \frac{V_0 T_k}{d_c}. (19)$$

The final, sixth dimensionless parameter, a/b, determines if friction is velocity weakening or velocity strengthening. The parameters P and Q can be understood as the dimensionless ratios of three characteristic shear stress changes. The stress change associated with the direct effect is $a\sigma_0$. Over the permeability evolution timescale T_k , slip V_0T_k accrues. Spatial variations of this slip with wavenumber $|\kappa|$ produce an elastic shear stress change $\mu^*|\kappa|V_0T_k/2$. Finally, the reduction in shear strength from the fault valve effect described at the end of the Introduction is $(\kappa f_0 q_0 \Delta k T_k)/(k_0 \beta \phi)$. This can be understood as follows. Linearization of the divergence of fluid flux term in (1) provides a term $(q_0/k_0)\partial k/\partial x \sim$ $q_0 \kappa \Delta k/k_0$, which is interpreted as the rate of fluid accumulation from spatial variations in fluid flux caused by spatial variations in permeability. Dividing the fluid accumulation rate by the specific storage $\beta\phi$ gives the pressurization rate. Multiplying this by the permeability evolution timescale T_k gives the pressure change, and multiplying this by f_0 gives the resulting reduction in shear strength. Thus, P compares the direct effect to the elastic stress change, and Q compares the strength reduction from fault valving to the direct effect. In addition, R quantifies the mitigating effect of pressure diffusion by comparing the diffusion length over the permeability evolution timescale, $\sqrt{c_0T_k}$, to the length scale of the perturbation κ^{-1} . M quantifies the dependence of permeability on effective stress by comparing the pressure change $\kappa q_0 T_k/(\beta \phi)$ to the stress sensitivity parameter σ^* . The pressure change is the fluid transported by steady flow at rate q_0 over timescale T_k , spread over the length scale κ^{-1} , divided by the specific storage $\beta \phi$. J is the ratio of the characteristic slip distance for permeability evolution (V_0T_k) to the state evolution distance d_c . P, R, M, J are always positive (for $\kappa > 0$). The sign of Q is the same as the sign of Δk , which in most cases is positive.

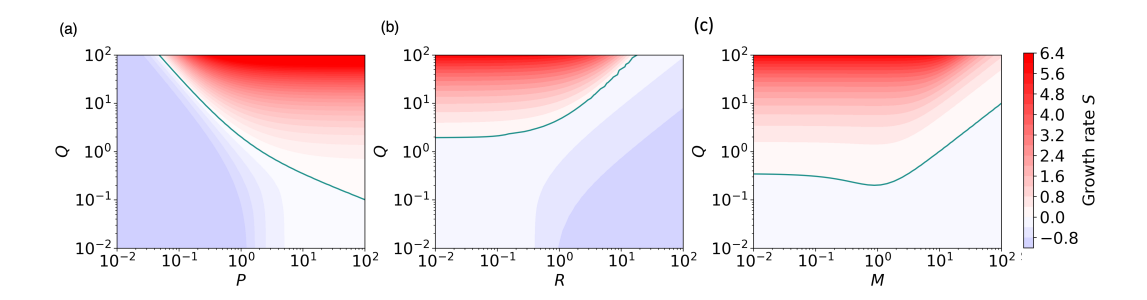


Figure 2. The maximum growth rate Re(S) calculated from equation (20). (a) P-Q space with R=1 and M=0. (b) R-Q space with P=1, R=0.01.

3.2 Fault valve instability: no state evolution limit

It is useful to neglect the state evolution effect as it separates the classical frictional instability that occurs for velocity-weakening friction. There are several ways to neglect the state evolution effects from (14). The first is to simply set b = 0, which yields

$$(PS+1)(S+1)(S+R+iM) + iPQS = 0. (20)$$

Even with non-zero b, state evolution is essentially negligible if J is either very small or very large. By taking the limit of $J \to 0$, we again obtain equation (20) because the permeability evolution time, and hence the fault valve instability, occurs over time scales much shorter than required for state evolution. The frictional response is the direct effect in this limit. For $J \gg 1$, state evolution is much faster than permeability evolution and friction is effectively always in steady state. This is similar to the previous limit but with a replaced with a-b (i.e., P and Q are replaced by Pa/(a-b) and Q(a-b)/a, respectively). This can be seen from the $J \to \infty$ limit of equation (14) (see Appendix).

Equation (20) has three complex solutions and we focus on the solution with the greatest real part as it dominates the system behavior. We plot $\max(\text{Re}(S))$ for various dimensionless parameters in Figure 2. Part of the parameter space exhibits unstable behavior, which we call the fault-valve instability. This instability is fundamentally different from the classical frictional instability arising from velocity-weakening friction, since we have already neglected state evolution and assumed a > 0. The system is most unstable for large values of Q and P. The diffusion parameter R has a stabilizing effect. Finally, the dependence on M is non-monotonic. For $M \ll 1$, the effective stress dependence of permeability is negligible. For M larger than unity, this process acts in a stabilizing manner. However, for $M \sim 1$, this process slightly enhances the instability.

3.3 Minimal conditions for the fault-valve instability

To find the minimal conditions for instability, we further neglect the effect of diffusion (R=0) and the effective stress dependence of permeability (M=0), as they are not essential for instability. Equation (20) simplifies to

$$(PS+1)(S+1) + iPQ = 0. (21)$$

This model accounts for fault valving (i.e., permeability evolution that leads to reductions in frictional strength through changes in fluid pressure), the direct effect, and elasticity.

Next we eliminate each of these processes one by one to identify which are essential for instability. Recall that P is the ratio of the direct effect to elasticity, and Q is the ratio of fault valving to the direct effect. Thus, PQ is the ratio of fault valving to elasticity, which is independent of the direct effect. If we neglect the direct effect in (21) by taking $P \to 0$ while keeping PQ finite, then sliding occurs at constant friction coefficient and we have retained only elasticity and fault valving. The solution is S = -1 - iPQ. Similarly, if we instead neglect permeability evolution in (21) (by taking $T_k \to 0$ so that permeability depends only on slip rate), then the solution is S = -1/P - iQ. (Note that all terms are proportional to T_k , which then cancels out). Both solutions in these extreme limits are always stable. It follows that the frictional direct effect (with a > 0), permeability evolution $(T_k > 0)$, and non-zero Q are required to generate the fault valve instability.

On the other hand, if we neglect elasticity in (21) by taking $P \to \infty$, we obtain the minimal condition for the fault-valve instability. The characteristic equation is

$$S^2 + S + iQ = 0. (22)$$

The two solutions depend only on a single parameter: Q. Figure 3 shows the solutions as a function of Q. There is an unstable mode and a stable mode. The unstable mode has a negative imaginary part, meaning the instability propagates in the direction of fluid flow (for $\Delta k > 0$). The other solution is always stable, and propagates in the opposite direction.

We examine the asymptotics for small and large Q. In the case of positive Δk , the solutions for $Q \ll 1$ are

$$S = -\frac{1}{2} \pm \left(\frac{1}{2} + Q^2 - iQ\right). \tag{23}$$

and the solutions for $Q \gg 1$ are

$$S = \pm \left(\sqrt{\frac{Q}{2}} - i\sqrt{\frac{Q}{2}}\right). \tag{24}$$

Therefore, the growth rate of one mode is always positive for all non-zero Q.

It is useful to discuss the instability in terms of wavelength of the perturbation, $\lambda = 2\pi/\kappa$. Equation (15) shows that we can write $Q = \kappa L_v$, where

$$L_v = \frac{f_0 q_0 \Delta k T_k}{k_0 \beta \phi a \sigma_0},\tag{25}$$

is the fault valve length scale. The asymptotic growth rate in the two limits above is

$$\operatorname{Re}(\mathbf{s}) = \begin{cases} \left(\frac{f_0 q_0 \Delta k \kappa}{2k_0 \beta \phi a \sigma_0 T_k}\right)^{\frac{1}{2}}, & \kappa \gg L_v^{-1}, \\ \frac{\kappa f_0 q_0 \Delta k}{k_0 \beta \phi a \sigma_0}, & \kappa \ll L_v^{-1}. \end{cases}$$
(26)

As can be seen in Figure 4, growth rate has a linear dependence on wavelength at short wavelengths, and square root dependence at long wavelengths.

The phase velocity of the instability, which is related to the propagation speed of the slip and fluid pressure pulse, is given by $V_{phase} = -\text{Im}(s)/\kappa$ with asymptotic behavior

$$V_{phase} = \begin{cases} \left(\frac{f_0 q_0 \Delta k}{2k_0 \beta \phi a \sigma_0 \kappa T_k}\right)^{\frac{1}{2}}, & \kappa \gg L_v^{-1}, \\ \frac{f_0 q_0 \Delta k}{k_0 \beta \phi a \sigma_0}, & \kappa \ll L_v^{-1}. \end{cases}$$
(27)

The phase velocity is asymptotically constant for large wavelengths.

If Δk is negative, the propagation direction of the modes are reversed while keeping the same growth rate. This is because q_0 and Δk appear only in the dimensionless parameter Q, and only as the product $q_0\Delta k$.

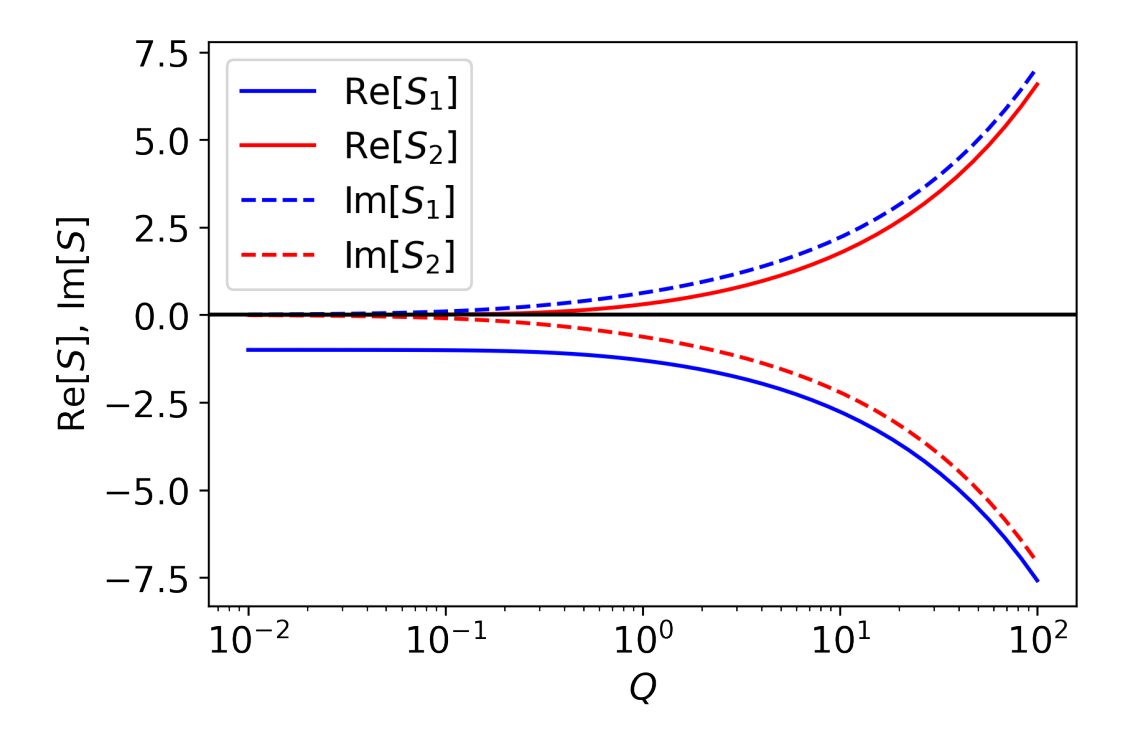


Figure 3. Two solutions of the characteristic equation (22). S_1 is the stable mode propagating in the opposite direction of fluid flow and S_2 is the unstable mode propagating in the direction of fluid flow.

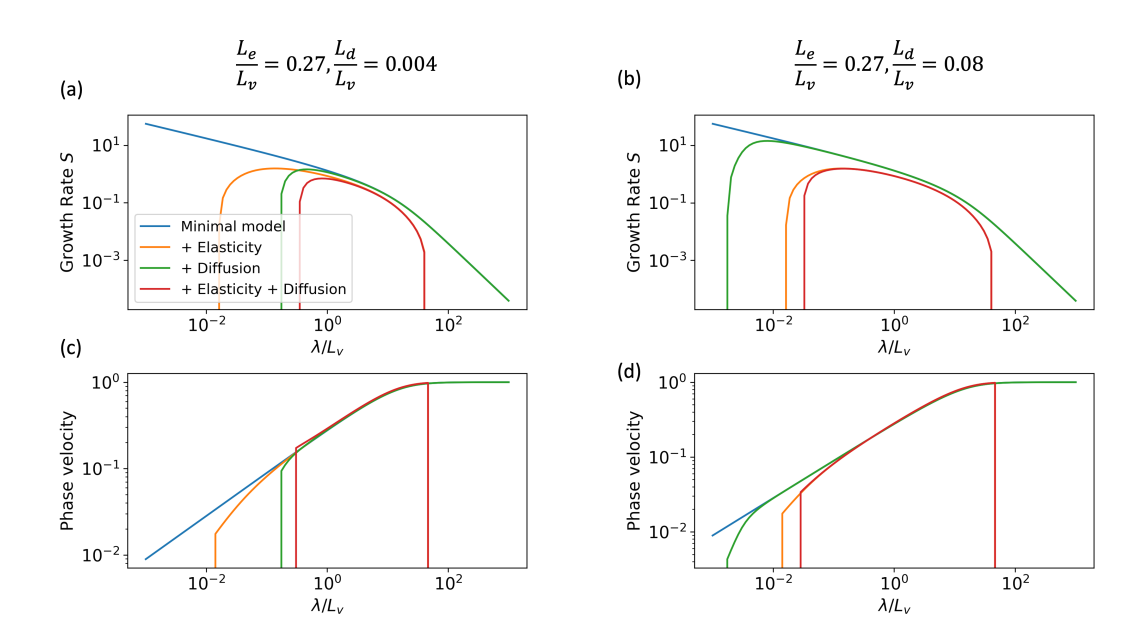


Figure 4. Growth rate Re(S) and phase velocity V_{phase} (normalized by $\frac{f_0q_0\Delta k}{k_0\beta\phi a\sigma_0}$) as a function of wavelength λ . Parameters are $k_0=10^{-15}~\text{m}^2$, $\Delta k=10^{-15}~\text{m}^2$, a=0.01, $\sigma_0=10$ MPa, $\mu=32.04$ GPa, $\nu=0.25$, $T_k=10^7$ s, $\beta=10^{-9}$ Pa⁻¹, $\phi=0.01$, $f_0=0.6$, $q_0=2\times10^{-8}$ m/s. Neglecting elasticity corresponds to setting $P^{-1}=0$. Neglecting diffusion corresponds to setting R=0. Both elasticity and diffusion are neglected in the minimal model.

3.4 Stabilizing effects of elasticity and diffusion

We have seen in the minimal model that all wavelengths are unstable and shorter wavelengths have higher growth rates. Now we add elasticity and diffusion, which have a stabilizing influence and lead to growth rate being maximized at a nonzero wavelength.

As with L_v , we introduce two additional length scales. First, we rewrite $P = (2\kappa L_e)^{-1}$, where

$$L_e = \frac{\mu^* V_0 T_k}{a \sigma_0},\tag{28}$$

is the characteristic length scale of elasticity. The other is related to diffusion. We write $R = (\kappa L_d)^2$, where

$$L_d = \sqrt{c_0 T_k} \tag{29}$$

is the hydraulic diffusion length. The relationship between L_v, L_e, L_d controls the wavelength dependence of the fault valve instability.

First we add elasticity while neglecting diffusion. The system is stable for all wavelengths when $L_e < L_v$. When $L_v < L_e$, then adding elasticity decreases the growth rate for all wavelengths, relative to the minimal model without elasticity, and stabilizes sufficiently short and long wavelengths. Between the two cutoff wavelengths that delimit this stability boundary, the growth rate is positive. We have analytical expressions for these neutrally stable wavelengths by solving equation (20), assuming S to be purely imaginary, which leads to

$$\lambda_e = \frac{\pi L_e^3}{(L_v \pm \sqrt{L_v^2 - L_e^2})^2}. (30)$$

Next we add diffusion while neglecting elasticity. The system is stable for all wavelengths when $L_v < L_d$. When $L_d < L_v$, then diffusion stabilizes only short wavelengths. The growth rate is positive for $\lambda > \lambda_d$, where

$$\lambda_d = 2\pi \sqrt{\frac{L_d^3}{L_v - L_d}},\tag{31}$$

which is confirmed by Figure 4.

Finally, we add both elasticity and diffusion. We consider two cases: $\lambda_e < \lambda_d$ and $\lambda_d < \lambda_e$ by changing the effective normal stress σ_0 . The upper limit of unstable wavelengths is controlled by elasticity, since diffusion stabilizes only short wavelengths. The lower limit can be controlled by either elasticity or diffusion.

The preferred wavelength (i.e., the one with maximum growth rate) is close to the minimum wavelength having a positive growth rate. The non-monotonic nature of the growth rate over wavelengths, in particular stability of long wavelengths, suggests that unstable slip takes the form of a slip pulse rather than a crack, as in Heimisson et al. (2019). Adding elasticity and/or diffusion does not significantly change the phase velocity (Figure 4). Thus, the maximum propagation speed of the instability is bounded by equation (27).

3.5 State evolution effects

To close this section, we return to the full model (including state evolution) to connect the fault valve model with the classical frictional instability. Figure 5 shows the growth rate as a function of a-b and wavelength. Two values of J are used by changing d_c . In the case of $J \ll 1$, state evolves much slower than permeability and a controls the

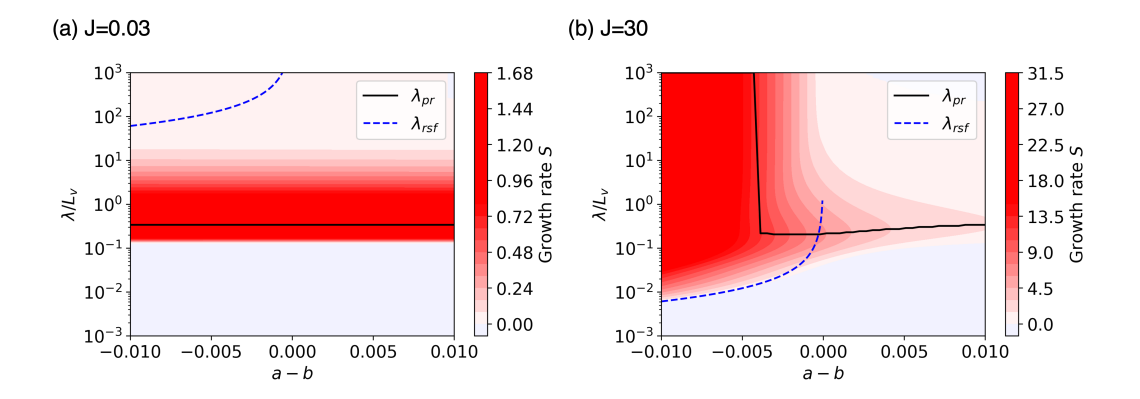


Figure 5. The effect of state evolution. (a) J=0.03 and (b) J=30. The dashed line is the critical wavelength $\lambda_c=\frac{\pi\mu^*d_c}{(b-a)\sigma_e}$ for a velocity-weakening fault with constant effective normal stress (Rice et al., 2001). Because a=0.010, the right edge of the horizontal axis corresponds to pure velocity-strengthening friction. The solid line is the preferred wavelength, λ_{pr} , and the dashed line marks the wavelength of neutral stability, λ_{rsf} for standard velocity-weakening rate and state friction. Note that λ_{pr} jumps to infinity for sufficiently negative a-b in (b). We used $d_c=10^{-6}$ m, and other parameters are identical to Figure 4.

instability as seen in section 3.2. In the case of $J\gg 1$, the behavior depends on a-b. The growth rate increases monotonically with λ for sufficiently negative a-b (velocity-weakening friction), except for negative a-b close to zero where there is still a finite wavelength of maximum growth rate. The minimum wavelength for instability is the critical wavelength given by $\lambda_{rsf} = \frac{\pi \mu^* d_c}{(b-a)\sigma_e}$ (Rice et al., 2001). That is, fault valving processes are of secondary importance and the instability is effectively the usual frictional instability. For positive a-b (velocity-strengthening friction), the fault valve instability produces unstable wavelengths with a preferred wavelength that depends on a-b.

4 Idealized Numerical Simulations

We have seen that velocity-strengthening faults can be unstable through the fault valve mechanism, but linear stability analysis alone does not reveal how the instability develops away from the steady state. Numerical simulations are required to explore the nonlinear dynamics of unstable slip. We use the specific permeability evolution law in equations (3) and (5). In addition, we examine how the finite fault length, which places an upper bound on the maximum wavelength of perturbations, affects the overall character of the solution.

4.1 Numerical Method

We use the quasi-dynamic boundary element method to calculate the elastic stress transfer on the fault (Rice, 1993), which is accelerated using H-matrices as detailed in S. Ozawa et al. (2023). We use the SBP-SAT finite difference method (Mattsson, 2012) to solve the fluid pressure diffusion equation (1) with variable coefficients. The diffusion equation is stiff and must be solved by an implicit method to avoid numerical instability when long time steps are used. We use an operator splitting scheme similar to Zhu et al. (2020). We use an explicit fifth order Runge-Kutta method for the time stepping of τ , ψ , and k^* . Slip rate V is calculated from equation (12) at each time step. The time step is adjusted with the relative error computed from the difference between the fifth and fourth order solutions (Press et al., 2002). Details can be found in S. Ozawa et al.

(2023). After updating τ , ψ , and k^* , we then time step equation (1) using the backward Euler method. We solve the sparse linear equation for the new pressure using the conjugate gradient method. Fixed point iteration is used to find a consistent solution between k^* and σ_e in equations (2) and (3). The accuracy of this method is first order in time due to the use of operator splitting, despite the fifth-order accuracy of the Runge-Kutta method. The mesh size is 25 m, and the result is very similar after a refinement to 12.5 m. We verified our code on the SEAS benchmark problem BP6 (https://strike.scec.org/cvws/seas/index.h for the special case of uniform diffusion coefficients.

To enhance the comparison with the linear stability analysis, we first consider the case of a planar fault with homogeneous parameters in an elastic whole space and neglect gravity (Figure 6a). The fault is loaded by constant creep at $V=V_0$ outside the computational domain by the backslip approach. The fluid pressures at both ends of the fault are set to values consistent with the steady-state flow rate q_0 and permeability k_0 , i.e., $p_r-p_l=L_f\eta q_0/k_0$, where L_f is the fault length. We also tested the Neumann boundary condition (fixed flow rate q_0 at the boundary) and got similar results except near the boundary. We set the total normal stress so that the background effective normal stress is uniform (i.e., $\sigma(x)=\sigma_0+p(x)$). We start a simulation by setting the initial slip rate 1% higher than the loading rate.

4.2 Example of spatiotemporal slip pattern

We first show a representative result with velocity-strengthening friction with no state evolution using the same parameters as Figure 4a. Figure 6 shows the space-time plots for slip rate, fluid pressure, permeability, and flow rate. We present our results in a non-dimensional form. There are aseismic slip events that span the entire fault domain. They take the form of a slip pulse rather than a crack, since only the tip of the rupture is sliding at any given time. The pulses propagate in the direction of the background fluid flow. The peak slip rate is about 20 times faster than the loading rate, much lower than the seismic slip rate that is limited by radiation damping. The propagation velocity of the slip pulse is nearly equal to the phase velocity for λ_{pr} derived from the linear stability analysis.

All variables are synchronized. When the slip front arrives, sudden fluid pressurization occurs as a result of the increase in fluid flow (Figures 6b-c). Weakening due to fluid pressurization, combined with the elastic stress concentration, accelerates slip at the pulse front (Figures 6b). However, slip acceleration increases permeability and hence fluid outflow (Figures 6d-e), limiting weakening by pressurization. Note that the weakening is driven by fluid pressurization alone, as there is no state evolution in this case and friction is velocity-strengthening.

4.3 Comparison with linear stability analysis

We perform a parameter space study for a-b and Q and plot the maximum slip rate V_{max} in Figure 7. Q is varied by changing q_0 with the other parameters fixed. $V_{max} = V_0$ indicates stable sliding and higher values indicate the occurrence of stick-slip. We see that the critical Q at the transition from stable sliding to stick-slip is quantitatively consistent with the linear stability analysis. In the unstable part of the positive a-b domain, the maximum slip rate increases slightly with flow rate, although it is still much slower than typical slip rates during earthquakes (\sim 1 m/s).

As a further comparison with the linear stability analysis, we vary the length of the fault, W (Figure 6a), using the same set of parameters (Figure 8). As expected, $W > \lambda_{min}$ is required to generate unstable slip. When W and λ_{pr} are of the same order, there are periodic slow slip events. When $W \gg \lambda_{pr}$, nonlinear effects are prominent. There is coalescence of two slip pulses during their propagation, since the propagation veloc-

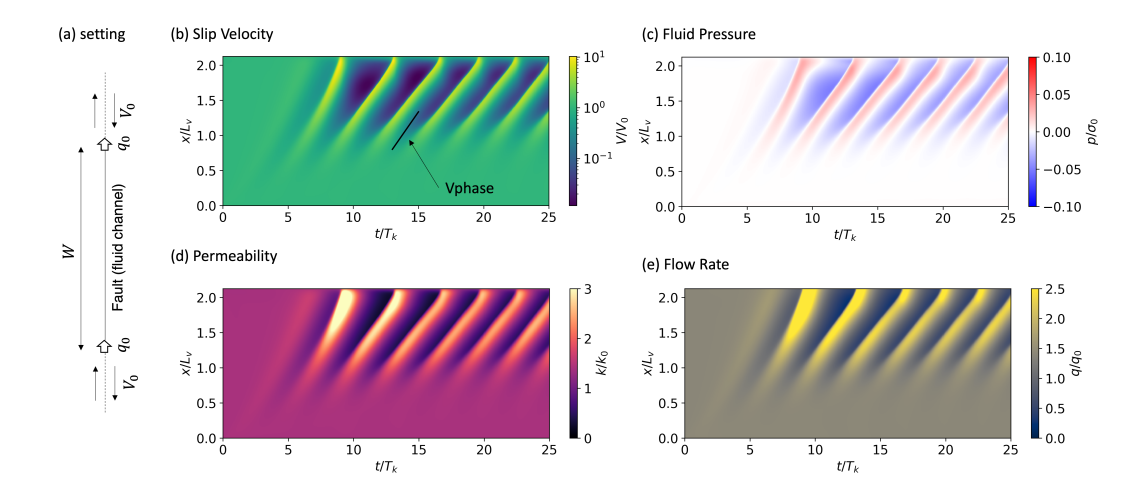


Figure 6. (a) Schematic of the idealized model. W is the fault length. (b-e) Space-time plot of slip rate, fluid pressure, permeability, flow rate for the idealized model. Parameters are shown in Table 1. Time and space axes are presented by a dimensionless manner using T_k and L_v , respectively, as defined in equations (A32) and (25). The phase velocity for the preferred wavelength calculated from the linear stability analysis is shown in the slope in (b).

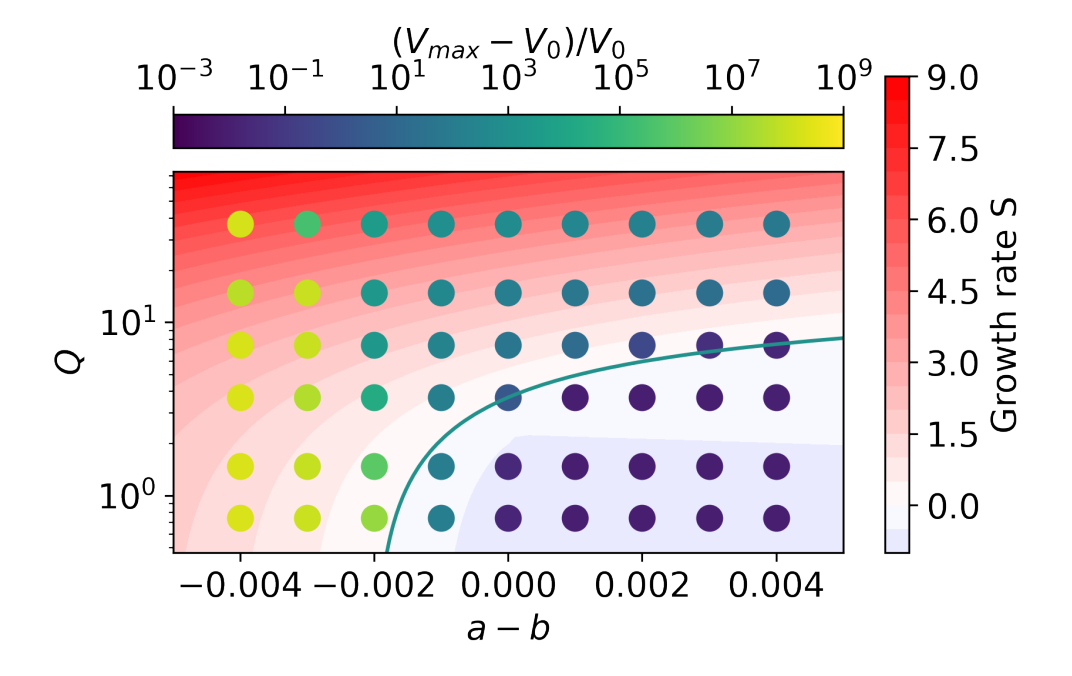


Figure 7. Comparison of numerical simulations and linear stability analysis. The color of each circle indicates the peak slip rate normalized by the loading rate. The background blue to red colors show the maximum growth rate computed from the linear stability analysis, and the solid line indicates the stability boundary. In numerical simulations, Q is varied by changing q_0 with other parameters fixed. For the linear stability analysis, we use $\lambda = 5$ km, which is the half of the fault length.

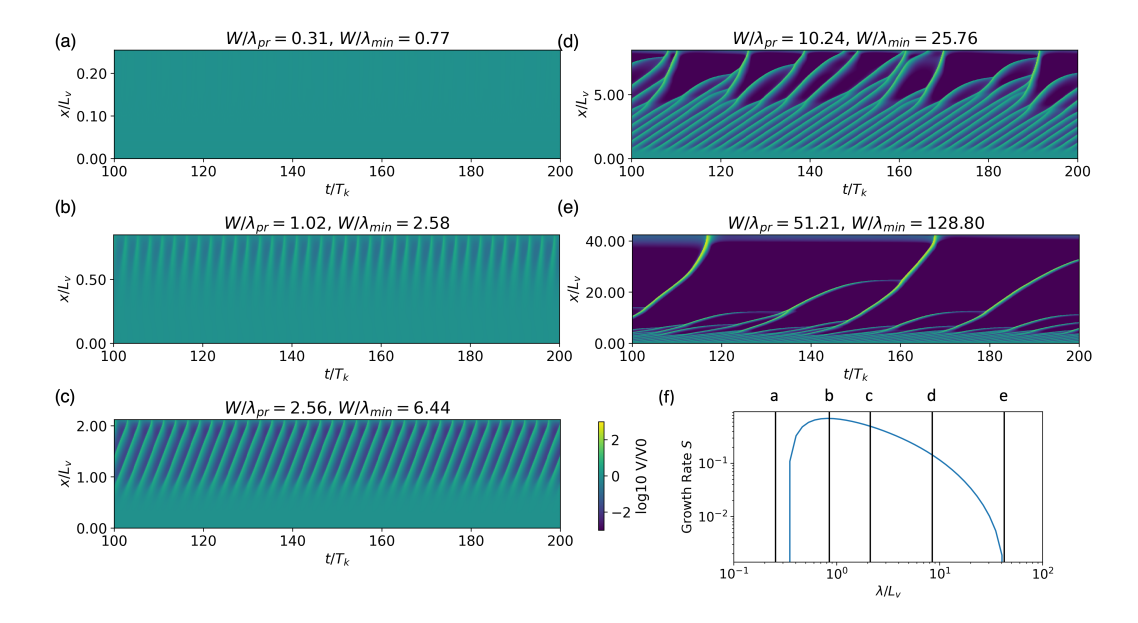


Figure 8. (a-e) Space-time plots of slip rate for different fault lengths. (f) Growth rate from linear stability analysis, with vertical black lines marking the fault length value corresponding to panels a-e. Stable creep occurs when $\lambda < \lambda_{min}$ and complex behavior with multiple slip pulses occurs when $\lambda \gg \lambda_{pr}$.

ity is not constant and typically much faster than predicted by the linear stability analysis. Consequently, the recurrence interval of slip at a given point on the fault is much longer for the low pressure (fluid outlet) side of the fault.

5 Subduction zone simulations

5.1 Model

We have shown the emergence of unstable aseismic slip and fluid pressure pulses due to the fault valve instability. One question is whether the parameters in real subduction zones are in a range that would produce the fault valve instability. In addition, the assumption of spatially uniform parameters is not valid for real tectonic settings. In this section, we perform earthquake cycle simulations on a subduction megathrust.

We consider depth-dependent physical properties such as a-b and permeability. The fault is 200 km long, embedded in an elastic half-space, and the dip angle is 15° (Figure 9a). We consider the effect of the free surface using the elastostatic Green function (Segall, 2010), but changes in fault normal stress are neglected when computing fault strength for simplicity. The normal stress change would only be significant in the shallowest region, and additional processes are likely important there that are not included in the model (e.g., inertial effects during rupture propagation, inelastic yielding, and a modified elastic response from compliant sediments). We present four models here, namely the reference model (Model A) and three models that change only one component from the reference (Models B-D). These are the frictional transition depth (Model B), the permeability (Model C), and the fluid sink (Model D).

The friction parameter a-b transitions from negative to positive (i.e., velocity-weakening to velocity-strengthening) at a certain depth, which sets the maximum depth

Table 1. Parameters for the simulation

Symbol	Description	Section 4	Section 5
$\overline{\mu}$	Shear modulus	32.04 GPa	32.04 GPa
ν	Poisson ratio	0.25	0.25
$ ho_r$	Density of rock		2600 kg/m^3
$ ho_f$	Density of fluid		1000 kg/m^3
g	Gravity acceleration		9.8 m/s^2
d_c	State evolution distance	1 mm	5 mm
V_0	Loading velocity	10^{-9} m/s	10^{-9} m/s
f_0	Reference friction coefficient	0.6	0.6
a	Direct effect	0.01	Depth-dependent (see Figure 9)
b	Evolution effect	Variable	0.01
L	Permeability evolution distance	1 m	5 mm
k_{max}	Maximum permeability	10^{-14} m^2	10^{-12} m^2
k_{min}	Minimum permeability	10^{-18} m^2	10^{-18} m^2
ϕ	Porosity	0.1	0.1
σ^*	Effective stress dependence of permeability		20 MPa
σ_0	Background effective normal stress	10 MPa	Depth-dependent (see Figure 9)
η	Fluid viscosity	10^{-4} Pa s	10^{-4} Pa s
β	Sum of the pore and fluid compressibility	10^{-9} Pa^{-1}	10^{-9} Pa^{-1}
q_0	Background flow rate	$2 \times 10^{-8} \text{ m/s}$	Depth-dependent (see Figure 9)
T	Healing time	$10^{7} { m s}$	Depth-dependent (see Figure 9)
T_0	Healing time for infinite temperature		$1.0 \mathrm{\ s}$
Q_a	Activation energy		83 kJ mol^{-1}
R_g	Gas constant		$8.3 \text{ J mol}^{-1} \text{ K}^{-1}$

extent of megathrust ruptures. The transition depth is 24 km for the reference Model A and 32 km for Model B (Figure 9e).

We assume that the permeability healing timescale has an Arrhenius-type dependence on temperature:

$$T = T_0 \exp(Q_a/R_g \Theta), \tag{32}$$

where T_0 is the reference healing time, Q_a is the activation energy, Θ is the absolute temperature, and R_g is the gas constant. We use values that fit well with the results of laboratory experiments measuring permeability evolution, such as Giger et al. (2007) and Morrow et al. (2001). Arrhenius-type fitting predicts very long T (greater than 1000 years) for low temperature (Figure 9b). The healing time at lower temperatures may be overestimated because temperature-insensitive healing mechanisms are neglected in our model. For example, the room temperature slide-hold-slide test in Im et al. (2019) showed an order of magnitude reduction in fracture permeability over a few hours. To relate depth to healing time T, we assume a linear geothermal gradient as $\Theta(z) = 300 + 12z$ K for depth z in km along the plate interface, which is motivated by the estimate in the Cascadia subduction zone (e.g., Van Keken et al. (2011)). However, we do not attempt to tune our model to reproduce slow slip events in the region. The distribution of T and T_k is shown in Figure 9c.

The model of Zhu et al. (2020) assumes that the fluid source is below the model domain, whereas we consider the fluid source within the model domain. In subduction zones, dehydration reactions occur over a wide depth range from the seismogenic zone to a few hundred kilometers depth (Hacker et al., 2003; C. B. Condit et al., 2020), suggesting that the maximum fluid production corresponds at least approximately to the depth of slow slip events. Calculation of the depth dependence of fluid flow rate, tak-

ing into account the dehydration reaction expected from the P-T path of subducting rocks, would be important for future work.

Fluids can flow into the upper plate if it is permeable. The permeability of the upper plate may vary significantly along dip due to changes in lithology. For example, Hyndman et al. (2015) proposed that the serpentinized mantle wedge corner has lower permeability and forces the fluid to flow along the plate interface. After passing the mantle wedge corner, the fluids can flow into the overriding plate.

For all models we add a fluid source at 41 km depth, which approximates fluid release from dehydration reactions in the oceanic lithosphere (Peacock, 1990). Fluid flow is confined to the fault interface in all models except in model D, where we add a fluid sink at 31 km depth following the conceptual ideas of Hyndman et al. (2015). The updip cumulative integral of the fluid sources and sinks results in the background flow distribution shown in Figure 9d. Other parameters are given in Table 1.

5.2 Steady state and linear stability

We obtain the depth profile of the steady state effective normal stress and permeability, as in previous studies (Rice, 1992; Zhu et al., 2020; Yang & Dunham, 2023; Kaneki & Noda, 2023). Here, we denote p as the absolute fluid pressure. Darcy's law provides the up-dip fluid flow rate,

$$q(x) = \frac{k}{\eta} \left(\frac{dp}{dx} - \rho_f g \sin \theta \right). \tag{33}$$

Using equations (2), (3), (6) and $\frac{d\sigma}{dx} = \rho_r g \sin \theta$, which approximates the total normal stress on the fault as lithostatic, the effective stress profile can be obtained by integrating

$$\frac{d\sigma_e}{dx} = (\rho_r - \rho_f)g\sin\theta - \frac{\eta q(x)}{k_{ss}^*(V_0; T(x))}e^{\sigma_e/\sigma^*},\tag{34}$$

where x is the along-dip distance, ρ_r is the density of the rock, and θ is the dip angle. The boundary condition at x = 0 is p = 0. The effective stress and permeability are determined in a self-consistent manner with the other hydraulic properties.

The calculated steady state σ_e and k for the four models are shown in Figure 9f-g. Increasing temperatures with depth decrease k and σ_e , since healing of permeability is more efficient. This feature was not observed for the depth-independent healing time (Zhu et al., 2020). The effective stress reaches $\sigma_e \sim 100$ MPa in the middle of the seismogenic zone in this setting due to our choice of higher permeability in Model A, but the value is lower for Model C using 20 times lower k_{max} (note that k_{max} is the permeability at the trench). The kink at 41 km depth corresponds to the drop in flow rate q associated with the fluid source. The permeability is similar between Models A and C except at shallow depths, despite the large difference in effective normal stress at deeper depths. For a fluid sink at the mantle wedge corner (Model D), the effective normal stress at downdip of the mantle wedge corner is lower than that of updip due to higher flow rate. Frictional properties do not affect either the effective normal stress or the permeability at steady state (Model B).

We also compute the growth rate Re(s) using linear stability analysis for a range of wavelengths (Figure 10). Both velocity-weakening and velocity-strengthening regions are unstable. The velocity-weakening region is the classical frictional instability with longer wavelengths being most unstable, while the velocity-strengthening region exhibits the fault-valve instability with the maximum growth rate around $\lambda \sim 20$ km. In Model C, the unstable wavelength is longer due to the small effective normal stress. In Model D, the growth rate is negative in the up-dip region of the mantle wedge corner, implying that slow slip events will not occur at these depths.

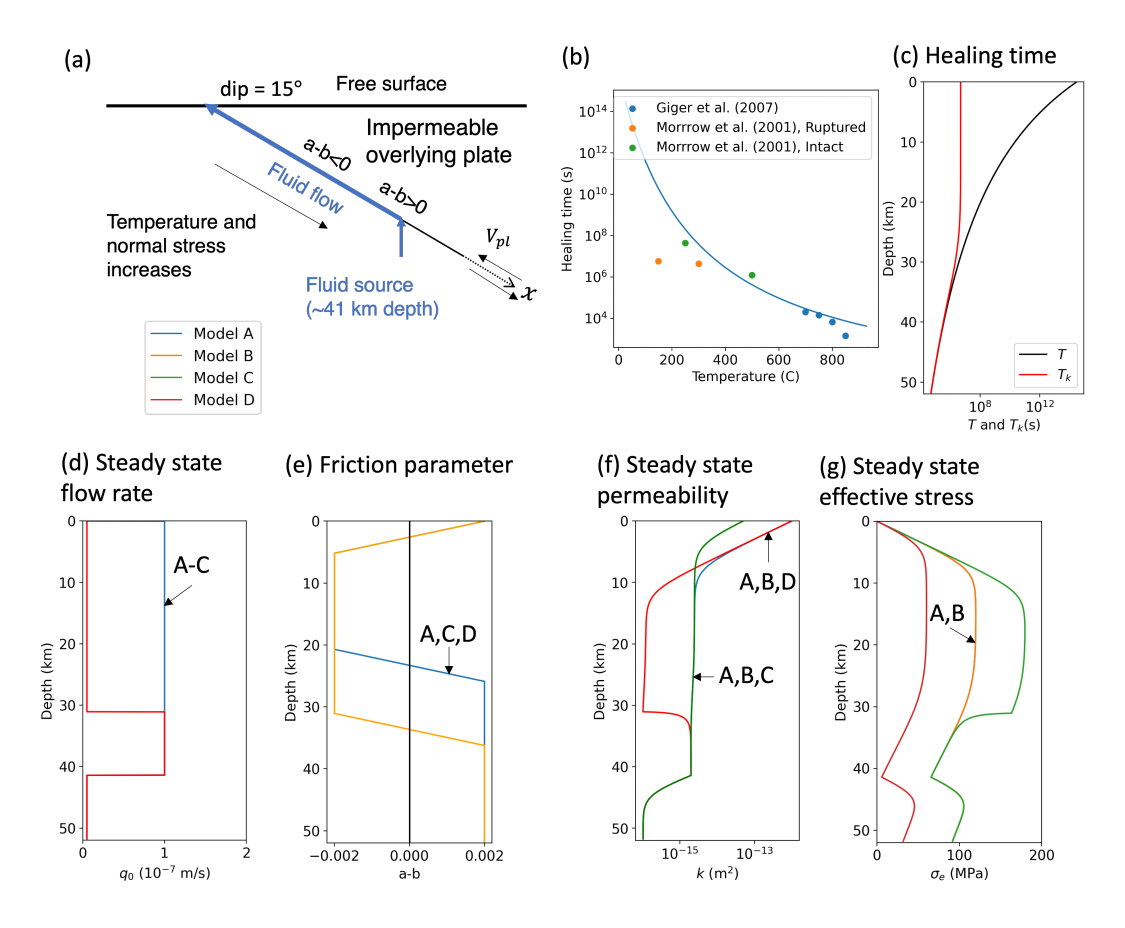


Figure 9. Subduction zone models. (a) Schematic illustration of the model setup. (b) Temperature dependence of the healing time T given by equation (32) with data from lab experiments. Depth profile of (b) T and T_k , (c) q, (d) a - b. The steady state solution obtained by integrating equation (34) is shown for (e) steady state permeability k and (f) steady state effective normal stress σ_e . Overlaps between different models are denoted in labels.

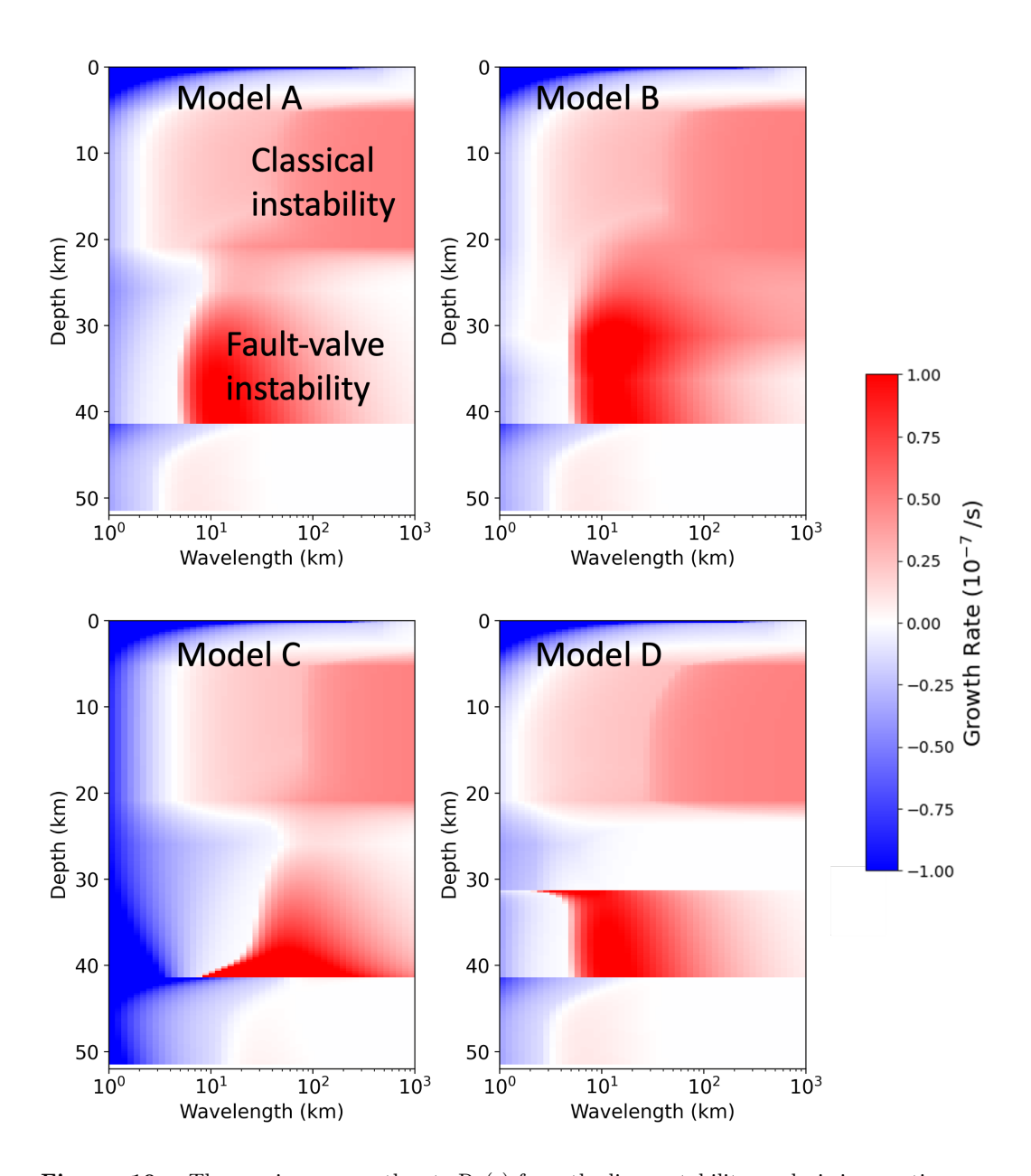


Figure 10. The maximum growth rate Re(s) from the linear stability analysis in equation (14) at each depth.

5.3 Simulation Results

733

734

735

736

737

738

739

742

743

746

747

748

749

750

751

754

755

756

757

758

759

761

762

763

766

767

768

770

771

772

773

775

776

777

779

780

781

782

783

We perform earthquake sequence simulations for the four model settings. Figure 11 shows the space-time plot of slip rate as well as the origin times and hypocenter locations from a synthetic earthquake catalog. An earthquake is defined when maximum slip rate is greater than $V_{th} = 10^{-2}$ m/s and its hypocenter is the location where the slip rate first exceeds V_{th} . The space-time plots are limited to 100 years, which includes one megathrust rupture that spans the full seismogenic zone. For Model A, Figure 12 shows time series for slip rate and effective normal stress at four depths before and after a megathrust earthquake. Figure 13 shows slip and shear stress for the same time period with Figure 12.

We start with Model A as a reference. Megathrust earthquakes have a recurrence interval of about 100 years. Many small earthquakes occur throughout the earthquake cycle in the seismogenic zone (between 5 km and 24 km depth) with most hypocenters between 10 km and 20 km depth. Numerous slow slip events with peak slip rates of 10^{-8} to 10^{-7} m/s occur at a depth range between 15 km and 35 km. The slow slip events begin in the velocity-strengthening region and propagate up-dip into the velocity-weakening region. Their propagation speed slows down when moving up-dip. This was not seen in the previous model using spatially uniform healing time (Zhu et al., 2020). While linear stability analysis predicts everywhere up-dip of the fluid source (42 km depth or 160 km along-dip) is unstable, the slow slip events initiate about 20 km up-dip of the fluid source. The stable slip near the fluid source is similar to what we have seen in Figure 8b,c and probably occurs because short wavelengths are stable and the fault length needs to be sufficiently long to create an instability. Also, the recurrence interval of slow slip events becomes longer when moving up-dip: a few months at 36 km depth and a few years at 26 km depth (Figure 12c-d, 13c-d). There are many examples of two slow slip events merging as they propagate up-dip, as in Figure 8d,e. The recurrence interval of slow slip events in Cascadia and Nankai also decreases with depth (Wech & Creager, 2011; Obara, 2010), although other models exist which explain the depth dependence of the recurrence interval by assuming a systematic decrease of effective stress with depth (Luo & Liu, 2021).

Unlike the uniform-T model which shows a gradual increase of the up-dip extent of slow slip late in the cycle (Zhu et al., 2020), the pattern of slow slip events as well as earthquakes in our model do not show significant changes over a seismic cycle. Small earthquakes at the base of the seismogenic zone migrate up-dip before a megathrust earthquake (Figure 11a). However, up-dip migration of seismicity frequently occurs and does not result in a megathrust earthquake in most cases.

In the source region of slow slip, the negative correlation between slip rate and effective normal stress is very clear (Figure 12c-d). In the seismogenic zone (Figure 12 a-b), the correlation is not clear as pore pressure is controlled by fluid input from deeper regions, which is in turn controlled by the slow slip events. The local variation in pore pressure in the slow slip region over a slow slip cycle is up to 10 MPa.

The slow slip events have slip of a few hundred millimeters (Figure 13), which is consistent with the long-term slow slip events in Nankai (Takagi et al., 2019). It is not straightforward to define the shear stress drop for these events. Since the fault-valve instability takes a form of slip pulse, shear stress drops once the pulse front arrives and recovers quickly (Figure 13c-d). Nevertheless, the shear stress difference before and after the passage of the rupture front is up to 2 MPa, which is much less than the nearly 10 MPa drop in fluid pressure (Figures 12 and 13). The model of Perez-Silva et al. (2023) also shows much larger changes in fluid pressure than shear stress.

In Model B (deeper transition depth of friction), slow slip events are observed at approximately the same depths as in Model A, although the duration of slip at a given location on the fault is shorter. There are sometimes regular earthquakes in the slow slip

region as friction is velocity-weakening. In Model C (low k_{max}), we still observe slow slip events at mostly similar depths compared to the reference Model A. The slow slip events show shorter recurrence intervals near the fluid source as predicted from the linear stability analysis (Figure 10).

In Model D (fluid sink at the mantle wedge corner), slow slip events are confined in the high flow rate region between the fluid source and sink. Up-dip of the mantle wedge corner, the flow rate is too small and the fault valve instability is disabled, as we observe from the linear stability analysis (Figure 10). There are many small earthquakes immediately before a large earthquake, but the seismicity is less active during the interseismic period than in other models. In addition, Model D shows longer and larger post-seismic slip down-dip of the seismogenic zone.

6 Discussion

784

785

788

789

790

793

794

795

796

797

798

799

800

803

804

805

807

808

810

811

812

813

814

815

816

817

818

819

820

821

823

824

825

826

827

831

832

833

6.1 Comparison with other models for slow slip

There is a large difference in the recurrence interval between megathrust earthquakes and slow slip in our Model A (Figure 11), even with relatively uniform effective normal stress. This is because earthquakes and slow slip events are the manifestation of two different mechanisms of instability. This contrasts with the rate-and-state model with constant (in time) fluid pressure (Liu & Rice, 2007; Matsuzawa et al., 2013; Barbot, 2019; Li & Liu, 2016), in which the slow slip events are the same instability as ordinary earthquakes, but near the stability boundary. The classical rate-and-state model requires very low (few MPa) effective normal stress in the slow slip region for the values of a-b adopted in most previous studies from laboratory friction experiments. This is much smaller than the tens to hundreds of MPa effective stress in the seismogenic zone, in order to produce the short recurrence interval of slow slip as compared to the megathrust earthquakes. These models impose the required effective stress distribution through a spatially compact region of extremely high pore pressure, which drops discontinuously or at least with an extreme gradient to a much smaller value in the seismogenic zone. These models provide little justification for how such extreme pressure gradients can be maintained without driving significant outflow, and hence depressurization, of the slow slip region. In our calculation of steady-state effective normal stresses, we show that locally high flow rate along the fault, and fluid loss from the megathrust above the slow slip region, is needed to produce an effective stress distribution similar to that assumed in Liu and Rice (2007) (Model D).

Several models incorporate the coupling between fluid pressure and slip and simulate the evolution of fluid pressure (Aochi et al., 2014; Dal Zilio & Gerya, 2022; Yamashita, 2013; Chen, 2023; Perez-Silva et al., 2023; Marguin & Simpson, 2023; Petrini et al., 2020; Heimisson et al., 2021; Dublanchet & De Barros, 2021; Hooker & Fisher, 2021). The way of inclusion is not unique and depends on the assumed process(es). A common way to account for fluids in modeling slow slip events is slip-induced dilatancy, which is neglected in our model. The fluid pressure suction due to slip-induced dilatancy stabilizes the system and expands the range of effective normal stresses that generate slow slip (Segall et al., 2010; Liu & Rubin, 2010; Sakamoto & Tanaka, 2022). Recently, Yang and Dunham (2023) added creep compaction of pores to dilatancy models. Their model produces slow slip events in the bottom portion and down-dip of the seismogenic zone. Their slow slip events are caused by the combination of low effective normal stress due to viscous compaction and the stabilizing effect of dilatancy on slip acceleration. However, the model still requires velocity-weakening friction. In contrast, velocity strengthening behavior is commonly observed at high temperatures in laboratory experiments using rocks commonly found at slow slip depths in subduction zones (Sawai et al., 2016; Okuda, Niemeijer, et al., 2023; Den Hartog et al., 2012).

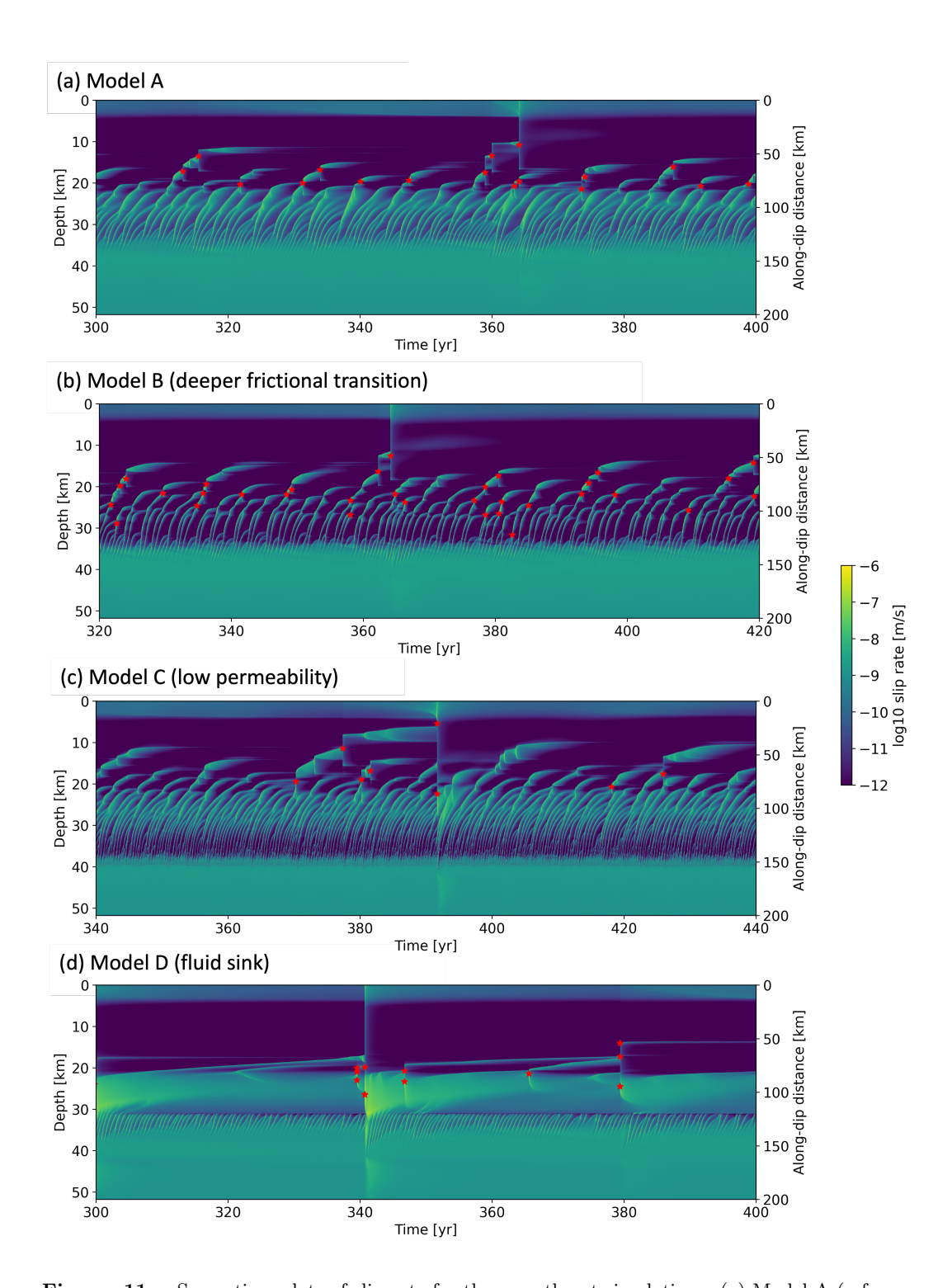


Figure 11. Space-time plots of slip rate for the megathrust simulations. (a) Model A (reference model) (b) Model B (deeper friction transition) (c) Model C (low permeability k_{max}). (d) Model D (fluid sink at the mantle wedge corner). Red stars indicate the hypocenters of earthquakes from the synthetic catalog.

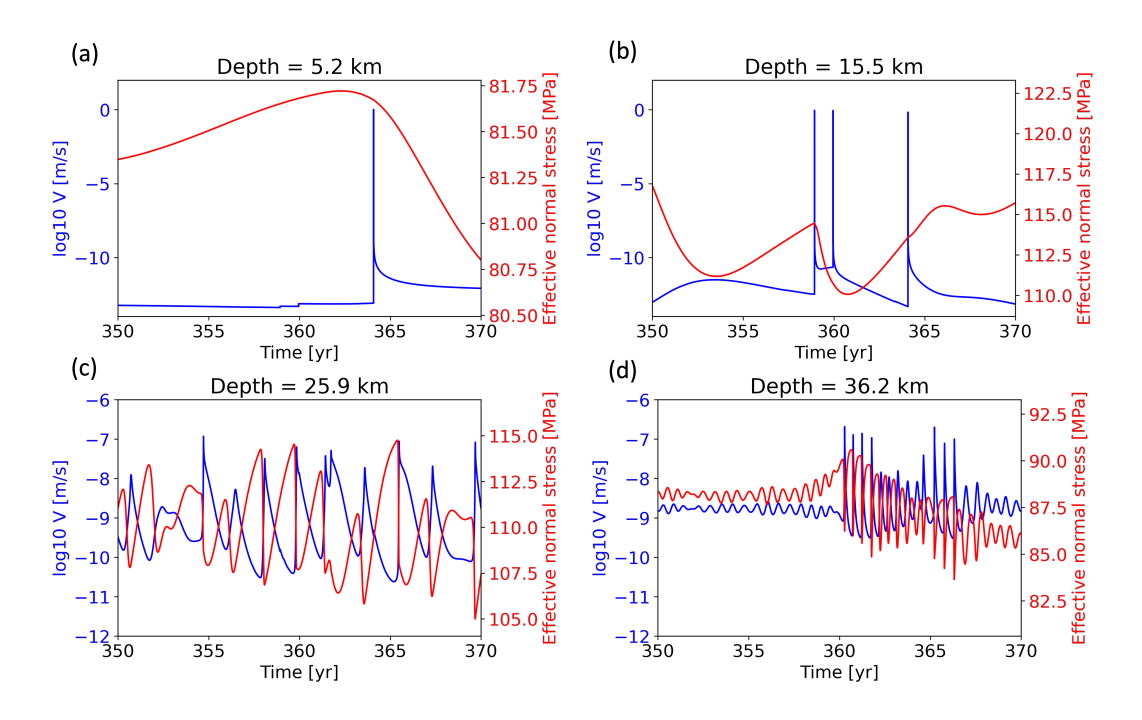


Figure 12. Time series of slip rate and effective normal stress at four locations for Model A. Note that full rupture of the seismogenic zone occurs at t = 364 years.

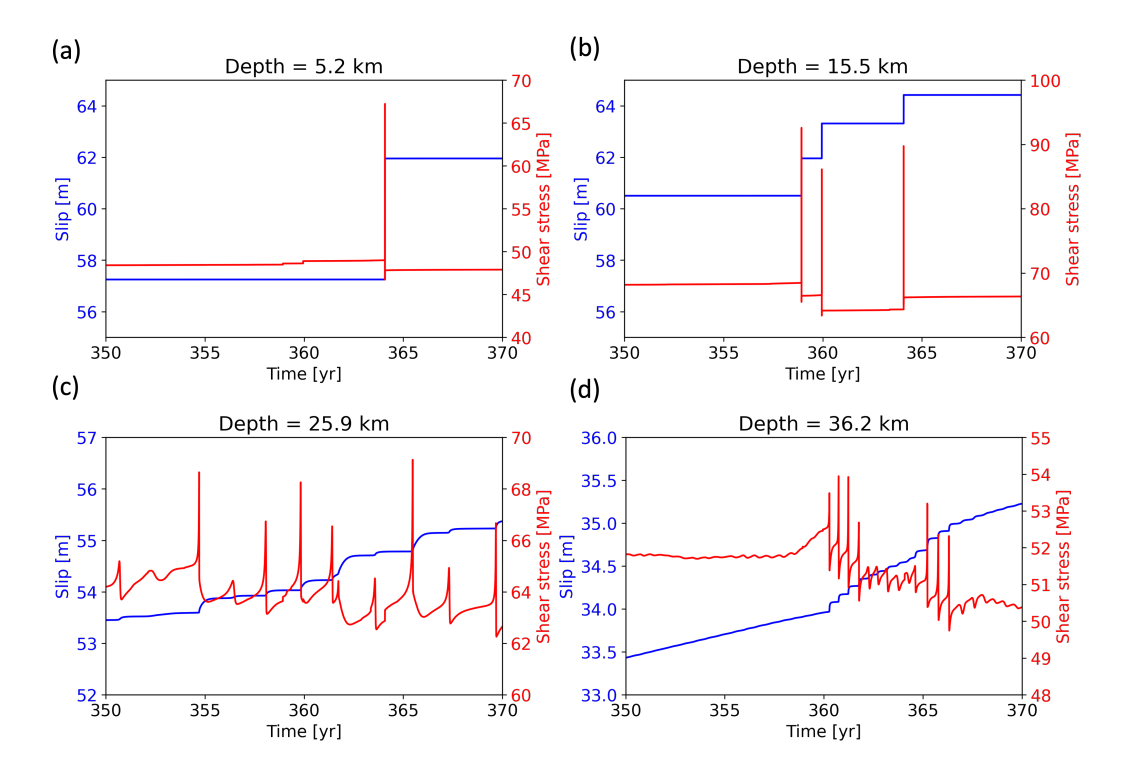


Figure 13. Time series of slip and shear stress at four locations for Model A. Note that full rupture of the seismogenic zone occurs at t = 364 years.

Perez-Silva et al. (2023) modeled slow slip events on velocity-strengthening faults in 3D, which occur in response to periodically imposed fluid pressure changes, and came to a similar conclusion that high permeability (or hydraulic diffusivity) is required to explain the observed source properties of slow slip in several subduction zones. Our model also produces slow slip events with velocity-strengthening friction, but the fluid pressure pulses arise spontaneously in our model as part of the internal dynamics of the system.

The fault-valve mechanism of slow slip is similar to the poroelastic bimaterial model of Heimisson et al. (2019), despite the conceptually different setting and governing equations. In their model, fluid pressure is coupled to slip through the undrained poroelastic response. When slip is localized on either side of the permeable fault core, symmetry breaking occurs. The direction of migration is determined by the location of the slip within the fault core. Their model better explains the existence of both up-dip and downdip migration of slow slip, which is what is observed in nature (Obara et al., 2012). In contrast, the fault valve instability produces along-flow and hence up-dip migration only (assuming permeability increases with slip rate). Ide (2012) shows that up-dip migration of tremor is more common in some subduction zones, but this trend is not universal. We do note that the fault valve instability remains unexplored in 3D, where its dynamics are likely more complex, and thus we have no predictions about observed slow slip properties like along-strike migration rate.

6.2 Constraints on hydrological parameters

The fault valve instability is sensitive to several hydrologic parameters, such as flow rate, permeability, specific storage, healing time, and permeability evolution distance. We discuss here how these can be constrained from geological and geophysical observations. The amount of fluid moving up-dip along the megathrust can be estimated. Thermodynamic modeling provides estimates of the volume of water released by metamorphic reactions as a function of depth (Peacock, 1990; C. B. Condit et al., 2020; McLellan et al., 2022). The hydration state of the subducting plate can be estimated seismologically (Canales et al., 2017). However, it is more difficult to estimate how much fluid is being diverted into the overriding plate rather than moving along the plate boundary. The flow paths are likely controlled by lithology and the presence or absence of splay faults in the overriding plates (Lauer & Saffer, 2015; Arai et al., 2023). As direct observations are difficult, geodynamic models for geological time-scale subduction are potentially useful to constrain the hydrological structure in the subduction zone (Menant et al., 2019; Wilson et al., 2014; Angiboust et al., 2012; Morishige & van Keken, 2017).

Hyndman et al. (2015) proposed that fluids flow primarily along the plate interface and, after passing the mantle wedge corner, ascend into the overriding plate. Therefore, we compared the simulation results with and without fluid loss at the mantle wedge corner. With fluid loss at the mantle wedge corner, we did not obtain slow slip events and small earthquakes up-dip of the mantle wedge corner, whereas there were active slow slip events and small earthquakes for the case without fluid loss at the mantle wedge corner. The observation in Cascadia is consistent with the fluid sink at the mantle wedge corner, since there is a gap between the locked zone and the region of episodic tremor and slip (Nuyen & Schmidt, 2021).

The flow rate (or Darcy velocity) q depends on the thickness of the fluid transport zone, even if the total volume of fluid moving along the plate boundary is the same. For the same volume rate (per unit distance along-strike) of fluid flow, Q_v , the flow rate $q = Q_v/w$ is inversely proportional to the width w of the fluid transport zone. The fault valve instability is enhanced for localized fluid transport zones as the dimensionless fault valve parameter Q is proportional to q. Hence, it is important to estimate the extent to which fluid flow is localized using rock records. For example, Ujiie et al. (2018) reports tens of meters thick zones of vein concentration in exhumed subduction zones.

In most slow slip models based on fluids (Perez-Silva et al., 2023; Cruz-Atienza et al., 2018; Skarbek & Rempel, 2016), very high permeability ($k \sim 10^{-12} \text{ m}^2$) compared to typical values for intact rock ($k \sim 10^{-18} \text{ m}^2$ (Katayama et al., 2012)) is required to match the migration speed of tremor. Much higher permeabilities than those of intact rock are possible when fractures subparallel to the plate boundary are well connected, as suggested from analysis of mineral veins in the rock record (Hosono et al., 2022; Muñoz-Montecinos & Behr, 2023). However, field-based approaches could overestimate permeability if the different veins were open at different times. Migration of seismicity also suggests a relatively high permeability (Talwani et al., 2007). However, estimates of permeability from seismic migration might be biased if stress transfer from earthquakes or aseismic slip is neglected, which has been shown to allow slip propagation at a much faster rate than pressure diffusion (Bhattacharya & Viesca, 2019). Thus, in-situ permeability in the slow slip source region is not well understood.

In subduction zones, it is likely that permeability is not a material property, but rather a quantity that dynamically adjusts with variations in the spatial density and connectivity of fractures. An important constraint follows from the fact that the fluid pressure gradient is limited by the lithostatic gradient. Quantitatively,

$$\frac{\partial p}{\partial x} < \rho_r g \sin \theta. \tag{35}$$

Using equation (33) and $q = Q_v/w$, we obtain

ana

$$kw > \frac{Q_v \eta}{(\rho_r - \rho_f)g\sin\theta}. (36)$$

Equation (36) illustrates that the product kw (also called hydraulic transmissivity) must be sufficiently large to accommodate the total volume of fluid flowing along the plate boundary that was created by metamorphic dehydration. The channel width may also be a dynamic quantity like permeability that adjusts in order to accommodate the volume rate of fluid flow (that is independently set by the fluid production rate). Specifically, the high fluid pressures in a very narrow channel would create fault-normal pressure gradients that drive fluids outward from the channel. The fluids might then increase the porosity and permeability of the rocks bounding the original channel, thereby expanding the channel. This would reduce the pressure in the channel while maintaining the same volume rate of flow. Ultimately the channel width will adjust to maintain pressures at a level below that required for channel expansion by microfracturing and similar processes.

We note that the effect of permeability on the propagation speed of fluid pressure in our model is very different from linear pressure diffusion. As seen from equation (27), the propagation speed scales with the relative permeability enhancement $\Delta k/k_0$. However, as discussed in the previous paragraph, flow rate q_0 and permeability k_0 are not independent. From equations (27) and (36), we have a rough estimate (for $\kappa L_v \ll 1$)

$$V_{phase} \sim \frac{f_0 \Delta k (\rho_r - \rho_f) g \sin \theta}{n \beta \phi a \sigma_0}.$$
 (37)

Therefore, the phase speed actually scales with Δk and appears to be independent of k_0 . However, we note that k_0 affects the background effective normal stress σ_0 , with low k_0 generally being associated with low σ_0 .

The duration of a slow slip event is approximately given by the length of the region hosting slow slip events divided by the phase velocity. A faster phase velocity leads to a shorter duration. In Model A, the phase velocity of the fault valve instability for $\lambda = 50$ km is 3×10^{-4} m/s at 30 km depth. On the other hand, the phase velocity for linear pressure diffusion is given by $V_{phase(lin)} = c_0 \kappa$. Substituting $\lambda = 50$ km and the hydraulic diffusivity at 30 km depth, $V_{phase(lin)} = 1.2 \times 10^{-5}$ m/s, which is much slower than the phase velocity of fault-valve instability. Thus, the fault-valve instability is a much faster mechanism for fluid pressure transport than linear pressure diffusion.

The growth rate and phase velocity of the fault valve instability also depend on porosity. The porosity relevant to our model is that of the fluid flow channel rather than the bulk rock. Seismic and electromagnetic imaging are often used to infer the spatial distribution of porosity (Naif et al., 2016; Peacock et al., 2011), but may not be able to resolve meter-scale vein concentration zones. In contrast, exhumed rocks could be used to investigate the permeability and porosity structure of the shear zone. For example, porosities of 1 to 10 % are estimated from rock records in the shear zone at the condition of deep slow earthquakes (Muñoz-Montecinos & Behr, 2023).

6.3 Limitations and future work

Our subduction zone simulations, shown in Figures 11-13, have some unrealistic features compared to the Cascadia observations. The duration of each slow slip event is longer than the slow slip recurrence interval. Consequently, part of the fault is always slipping. In contrast, slow slip events at Cascadia have durations of a few weeks and recurrence intervals of about a year (Rogers & Dragert, 2003). It is not currently clear whether this issue can be resolved by changing parameters or whether the model needs to be modified. Future work should test if the model can be tuned to reproduce the various observations of slow slip events and megathrust earthquakes.

We have focused on the slow slip events in the deeper extension of the seismogenic zone. Due to the recent development of seafloor geophysical observations, slow slip events are also detected in the shallow megathrust near the trench (Nakano et al., 2018; Nishikawa et al., 2019). Our subduction simulations did not produce shallow slow slip events due to the choice of the long healing time in that region. If there are additional healing processes that can operate at these colder temperatures and shallower depths, then shallow slow slip events might also be explained by the fault valve instability.

An important requirement for the fault valve instability is that the pore pressure must be related to the shear strength, and hence slip rate, via the effective stress law. If shear deformation is accommodated by viscous creep with weak pore pressure dependence of viscosity, then a change in pore pressure does not result in a change in slip rate. Models also explain slow slip events based on viscous rheology (Ando et al., 2012), sometimes with thermal coupling (Goswami & Barbot, 2018). However, the existence of seismic signals of slow slip events (i.e., tremor and low frequency earthquakes) suggests that at least part of the deformation in slow slip events is frictional. Field observations of rocks recording deformation at the pressure and temperature conditions of slow earthquakes show heterogeneous structures exhibiting both frictional and viscous deformation (Behr & Bürgmann, 2021; Kirkpatrick et al., 2021). Models simulating both frictional and viscous deformation in a finite thickness shear zone are emerging (Behr et al., 2021; Lavier et al., 2021), but thus far these neglect fault valving and fluid pressure effects.

Our 2D along-dip simulations do not address the observed along-strike migration of slow slip events. This raises two questions. First, is there background flow in the along-strike direction? Along-strike heterogeneity in dehydration sources related to thermal structure is a possible explanation for its existence (McLellan et al., 2022). Recently, Farge et al. (2023) explained the along-strike migration of tremor by a fault valve type model with along-strike variation of permeability. In contrast, our model focuses on how heterogeneity in permeability and pore pressure arises from internal dynamics starting from a uniform initial state. The two models might be complementary.

Second, even without background flow in the along-strike direction, could 3D dynamics generate along-strike migration of slow slip events? Elastic stress transfer could explain the along-strike migration of slow slip, as discussed by Heimisson et al. (2019). Seismological observations of tremor as diagnostic of slow slip events show that relatively slow along-strike migration of slow slip events is often accompanied by much faster along-dip migration (Ghosh et al., 2010; Obara et al., 2012; Ide, 2012). Several models have

attempted to explain this observation. For example, Rubin (2011) proposed a friction law capable of producing a bimodal propagation velocity using two state variables. Ando et al. (2010) reproduced the difference in migration speed along-strike and along-dip by assuming anisotropic heterogeneity in brittle patches.

The permeability evolution law needs to be elaborated by comparison with experimental observations as well as microphysical modeling. Our model predicts that the steady state permeability is proportional to the slip velocity (equation (6)), even away from the steady state, which may overestimate the effect of permeability enhancement. For example, experiments in a granite fracture show much smaller permeability enhancement after velocity jumps than our model (Ishibashi et al., 2018). The permeability evolution law away from the steady state will influence the nonlinear dynamics of the slip pulse, including the peak slip rate.

7 Conclusions

In this work, we studied the dynamics of fault slip with coupling between slip, permeability, fluid flow, and fluid pressure. Using linear stability analysis, we showed that steady slip and fluid flow is unstable to perturbations for sufficiently high background flow rate and degree of permeability enhancement. We identified six dimensionless parameters that control the stability of the system. The fault-valve instability occurs even with pure velocity-strengthening friction, but it is eliminated when the direct effect is removed (i.e., sliding occurs at constant friction coefficient) or the permeability responds instantaneously to the slip velocity. The growth rate and phase speed scale with the permeability enhancement.

Numerical simulations show that the fault valve instability takes the form of unidirectional propagation of an aseismic slip pulse and fluid pressure pulse. The recurrence interval scales with the time scale of permeability evolution, and the propagation velocity and recurrence interval are consistent with the prediction from the linear stability analysis. When the system size is much larger than the preferred wavelength, multiple aseismic slip pulses merge during propagation and the dynamics become more complex.

We have also performed earthquake sequence simulations for subduction megathrusts with depth-dependent parameters. Using the healing time T empirically derived from laboratory experiments and assuming a representative geotherm for subduction zones with deep slow slip events, the simulations spontaneously generated slow slip events (via the fault valve instability) from the lower portion of the seismogenic zone to the downdip extension. The slow slip events occur in both velocity-weakening and velocity-strengthening regions. The distributions of effective normal stress and permeability are determined in a self-consistent manner, so we do not have to impose some ad hoc distribution of effective normal stress like in almost all other models for slow slip. Lower permeability near the trench results in lower effective normal stress at the source depth of slow slip. Under this condition, slow slip events have shorter recurrence intervals. The introduction of a fluid sink at the corner of the mantle wedge confines slow slip events to down-dip of the corner and explains the separation between the extent of megathrust rupture and the region of slow slip. This highlights the importance of determining the amount of fluid discharge into the upper plate.

Some characteristics of slow slip, such as the absence of quiescent periods due to the slow migration rate relative to the recurrence interval and the absence of down-dip migration, are inconsistent with observations in Cascadia. In the future, we plan to study how this instability is manifested in 3D to address both along-dip and along-strike migration of slow slip events. We also plan to relax certain assumptions made in this study, such as constant porosity and the neglect of fault-normal flow.

Finally, the potential relevance of the fault-valve instability is not limited to subduction zone slow slip events. Aseismic slip is observed on continental strike-slip faults (Bilham, 1989; Wei et al., 2013; Materna et al., 2024; Khoshmanesh & Shirzaei, 2018). Aseismic slip is also important for injection-induced seismicity (Bhattacharya & Viesca, 2019; Guglielmi et al., 2015). Injection-induced aseismic slip is well studied for constant permeability (Dublanchet, 2019; Sáez et al., 2022), but the fault-valve instability might lead to more complex dynamics.

8 Open Research

The code HBI used in the numerical simulations is found at Zenodo (S. Ozawa, 2024b). Input files and scripts to generate figures are found at Stanford Digital Repository (S. Ozawa, 2024a).

Appendix A Derivation of linear stability analysis

A1 Fluid pressure diffusion equation

The fluid pressure diffusion equation is

$$\beta \phi \frac{\partial p}{\partial t} - \frac{\partial}{\partial x} \left(\frac{k}{\eta} \frac{\partial p}{\partial x} \right) = 0. \tag{A1}$$

We decompose p and k into the superposition of a steady state value and perturbation, denoted with subscript 0 and prime, respectively:

$$\beta \phi \frac{\partial (p_0 + p')}{\partial t} - \frac{\partial}{\partial x} \left(\frac{k_0 + k'}{\eta} \frac{\partial (p_0 + p')}{\partial x} \right) = 0.$$
 (A2)

We assume that k_0 is uniform. Opening brackets and neglecting second-order terms, we obtain

$$\beta \phi \frac{\partial p'}{\partial t} - \frac{k_0}{\eta} \frac{\partial^2 p'}{\partial x^2} + \frac{q_0}{k_0} \frac{\partial k'}{\partial x} = 0, \tag{A3}$$

where we made use of the definition of steady flow rate

$$q_0 = -\frac{k_0}{\eta} \frac{\partial p_0}{\partial x}.$$
 (A4)

We apply Laplace transform in time $(\frac{\partial p'}{\partial t} \to s\hat{p}')$ and Fourier transform in space $(\frac{\partial p'}{\partial x} \to i\kappa\hat{p}')$. This means we assume $\exp(st+i\kappa x)$ dependence in x and t. Then, we get

$$\beta \phi s \hat{p}' + \frac{k_0}{\eta} \kappa^2 \hat{p}' + \frac{q_0}{k_0} i \kappa \hat{k}' = 0, \tag{A5}$$

and we denote the hydraulic diffusivity at steady state as

$$c_0 = \frac{k_0}{\beta \phi \eta}. (A6)$$

A2 Permeability evolution equation

We assume that permeability depends on the instantaneous effective normal stress,

$$k = k^* f(\sigma_e) \tag{A7}$$

and the evolution law depends on permeability and slip rate,

$$\frac{dk^*}{dt} = g(k^*, V). \tag{A8}$$

Equations (A7) and (A8) are combined to eliminate k^* , yielding

$$\frac{dk}{dt} = A(k, \sigma_e) \frac{d\sigma_e}{dt} + B(k, \sigma_e, V), \tag{A9}$$

1070 where

$$A(k, \sigma_e) = k \frac{df(\sigma_e)/d\sigma_e}{f(\sigma_e)}$$
(A10)

 $_{072}$ and

1071

1073

1076

1077

1078

1079 1080

1081

1082

1083

1084

1085

1086

1087

1088

1089

1090

1091

1092

1093

1095

$$B(k, \sigma_e, V) = f(\sigma_e)g\left(\frac{k}{f(\sigma_e)}, V\right). \tag{A11}$$

Steady state requires $B(k, \sigma_e, V) = 0$, which implicitly defines the steady state permeability function $k = k_{ss}(V, \sigma_e)$.

We denote $k_0 = k_{ss}(V_0, \sigma_0)$ and then linearize equation (A9) and the steady state permeability function $k_{ss}(V, \sigma_e)$ to obtain

$$\frac{dk}{dt} = -\frac{k_0}{\sigma^*} \frac{d\sigma_e}{dt} - \frac{1}{T_k} [k - k_{ss}^{lin}(V, \sigma_e)], \tag{A12}$$

$$k_{ss}(V, \sigma_e) = k_0 - k_0 \frac{\sigma_e - \sigma_0}{\sigma^*} + \Delta k \frac{V - V_0}{V_0}, \tag{A13}$$

where we have defined several parameters as follows. The timescale for permeability evolution, T_k , is defined via

$$T_k^{-1} = -\left. \frac{\partial B(k, \sigma_e, V)}{\partial k} \right|_{(k_0, \sigma_0, V_0)},\tag{A14}$$

the permeability enhancement is

$$\Delta k = V_0 \left. \frac{\partial k_{ss}(V, \sigma_e)}{\partial V} \right|_{(V_0, \sigma_0)},\tag{A15}$$

and the stress sensitivity parameter is

$$\sigma^* = -\frac{k_0}{A(k_0, \sigma_0)} = -\left. \frac{f(\sigma_e)}{df(\sigma_e)/d\sigma_e} \right|_{\sigma_0}.$$
 (A16)

In the Fourier-Laplace domain, the perturbed variables follow

$$\left(s + \frac{1}{T_k}\right)\hat{k}' = \frac{k_0}{\sigma^*} \left(s + \frac{1}{T_k}\right)\hat{p}' + \frac{\Delta k s \hat{\delta}'}{V_0 T_k},\tag{A17}$$

where we used $\hat{\delta}' = \hat{V}'/s$ to denote the transform of the slip perturbation δ' .

A3 Rate and state friction and static elasticity

The linearized rate and state friction law is (Rice et al., 2001)

$$\frac{\mathrm{d}\tau}{\mathrm{d}t} = \frac{a\sigma_0}{V_0} \frac{\mathrm{d}V}{\mathrm{d}t} + f_0 \frac{\mathrm{d}\sigma_e}{\mathrm{d}t} - \frac{V_0}{d_c} \left[\tau - \tau_{ss}(\sigma_e, V)\right],\tag{A18}$$

where the steady-state shear strength is given by

$$\tau_{ss}(\sigma_e, V) = \tau_0 + f_0(\sigma_e - \sigma_0) + \frac{(a-b)\sigma_0}{V_0}(V - V_0). \tag{A19}$$

In the perturbed state, equations (A18) and (A19) are combined as

$$\frac{\mathrm{d}\tau'}{\mathrm{d}t} = \frac{a\sigma_0}{V_0} \frac{\mathrm{d}V'}{\mathrm{d}t} - f_0 \frac{\mathrm{d}p'}{\mathrm{d}t} - \frac{V_0}{d_a} \left[\tau' + f_0 p' - \frac{(a-b)\sigma_0}{V_0} V' \right]. \tag{A20}$$

Performing the Fourier-Laplace transforms and rearranging, we obtain

$$\left(s + \frac{V_0}{d_c}\right)\hat{\tau}' = -f_0\left(s + \frac{V_0}{d_c}\right)\hat{p}' + \sigma_0\left(\frac{a}{V_0}s^2 + \frac{a-b}{d_c}s\right)\hat{\delta}'.$$
(A21)

Slip and shear stress are also related by static elasticity (e.g., Rice et al. (2001))

$$\hat{\tau}' = -\frac{\mu^* |\kappa|}{2} \hat{\delta}'. \tag{A22}$$

where $\mu^* = \mu$ for antiplane shear and $\mu^* = \mu/(1-\nu)$ for plane strain.

A4 Characteristic equation

1098

1099

1100

1101

1102

1103

1104 1105

1107 1108

1109

1110

1112

1114

1115

1117

1120

1121

1122

1123

1125

1126

1127

1128

1130

Now we combine equations (A5), (A17), (A21), and (A22) to get

 $\left(s+\frac{V_0}{d_s}\right)\frac{\mu^*}{2}|\kappa|+\sigma_0\left(\frac{a}{V_0}s^2+\frac{a-b}{d_s}s\right)$ $+\frac{i\kappa f_0 q_0 \Delta k s(s+V_0/d_c)}{k_0 \beta \phi V_0 T_k(s+1/T_k)(s+c_0 \kappa^2 + i\kappa q_0/\sigma_0^* \beta \phi)} = 0.$

This is the characteristic equation that relates the growth rate s and wavenumber κ .

We nondimensionalize the characteristic equation (A23). We take $s = S/T_k$ and rewrite (A23) as

$$PS^{2} + \left(\frac{a-b}{a}PJ + 1\right)S + J + iPQ\frac{S(S+J)}{(S+1)(S+R+iM)} = 0.$$
 (A24)

with five dimensionless parameters defined as follows: 1113

$$P = \frac{2a\sigma_0}{\mu^* |\kappa| V_0 T_k},$$

$$Q = \frac{\kappa f_0 q_0 \Delta k T_k}{k_0 \beta \phi a \sigma_0},$$

$$R = c_0 \kappa^2 T_k,$$
(A25)
(A26)

$$Q = \frac{\kappa J_0 q_0 \Delta \kappa I_k}{k_0 \beta \phi a \sigma_0},\tag{A26}$$

$$R = c_0 \kappa^2 T_k, \tag{A27}$$

$$M = \frac{\kappa q_0 T_k}{\sigma^* \beta \phi},\tag{A28}$$

$$J = \frac{V_0 T_k}{d_c}. (A29)$$

See the main text for the physical meaning of these parameters. Note that a/b is the sixth dimensionless parameter of the problem.

If we use the specific permeability evolution law of Zhu et al. (2020),

$$g(k^*, V) = \frac{V}{L}(k_{\text{max}} - k^*) - \frac{1}{T}(k^* - k_{\text{min}}), \tag{A30}$$

and effective stress dependence function 1124

$$f(\sigma_e) = e^{-\sigma_e/\sigma^*},\tag{A31}$$

then we obtain from (A14) and (A15)

$$T_h^{-1} = 1/T + V_0/L, (A32)$$

$$T_k^{-1} = 1/T + V_0/L,$$

$$\Delta k = \frac{V_0 T_k^2 k_{max} e^{-\sigma_0/\sigma^*}}{TL} = \frac{V_0 T_k}{L} \left(k_{max} e^{-\sigma_0/\sigma^*} - k_0 \right).$$
(A32)

We also note that σ^* coincides with the definition given in (A16).

A5 Limits of negligible state evolution

State evolution is negligible when J is either very large or small. For $J\ll 1,$ equation (A24) yields

$$PS + 1 + \frac{iPQS}{(S+1)(S+R+iM)} = 0.$$
 (A34)

For $J \gg 1$, we divide equation (A24) by J:

$$J^{-1}PS^{2} + \left(\frac{a-b}{a}P + J^{-1}\right)S + 1 + iPQ\frac{S(J^{-1}S+1)}{(S+1)(S+R+iM)} = 0,$$
(A35)

and then we assume $J^{-1} \to 0$ to obtain

$$\frac{a-b}{a}PS + 1 + \frac{iPQS}{(S+1)(S+R+iM)} = 0. (A36)$$

In this case, by replacing a with a - b in the definition of P and Q, we recover equation (A34).

Acknowledgments

We thank the three anonymous reviewers for their useful comments. S.O. was partially funded by a Japan Society for the Promotion of Science (JSPS) Overseas Fellowship and Oversea Research Supports from the Yamada Science Foundation. Y.Y. was supported by the Research Grants Council Postdoctoral Fellowship, University Grants Committee, Hong Kong (PDFS2223-4S08) and the Faculty of Science at the Chinese University of Hong Kong. This work was also supported by the National Science Foundation (EAR-1947448 to E.M.D.).

References

- Ando, R., Nakata, R., & Hori, T. (2010). A slip pulse model with fault heterogeneity for low-frequency earthquakes and tremor along plate interfaces. *Geophysical Research Letters*, 37(10).
- Ando, R., Takeda, N., & Yamashita, T. (2012). Propagation dynamics of seismic and aseismic slip governed by fault heterogeneity and newtonian rheology. *Journal of Geophysical Research: Solid Earth*, 117(B11).
- Angiboust, S., Wolf, S., Burov, E., Agard, P., & Yamato, P. (2012). Effect of fluid circulation on subduction interface tectonic processes: Insights from thermomechanical numerical modelling. Earth and Planetary Science Letters, 357, 238–248.
- Aochi, H., Poisson, B., Toussaint, R., Rachez, X., & Schmittbuhl, J. (2014). Self-induced seismicity due to fluid circulation along faults. *Geophysical Journal International*, 196(3), 1544–1563.
- Arai, R., Miura, S., Nakamura, Y., Fujie, G., Kodaira, S., Kaiho, Y., ... others (2023). Upper-plate conduits linked to plate boundary that hosts slow earth-quakes. *Nature Communications*, 14(1), 5101.
- Barbot, S. (2019). Slow-slip, slow earthquakes, period-two cycles, full and partial ruptures, and deterministic chaos in a single asperity fault. *Tectonophysics*, 768, 228171.
- Barbot, S. (2023). Constitutive behavior of rocks during the seismic cycle. AGU Advances, 4(5), e2023AV000972.
- Bar-Sinai, Y., Spatschek, R., Brener, E. A., & Bouchbinder, E. (2014). On the velocity-strengthening behavior of dry friction. *Journal of Geophysical Research: Solid Earth*, 119(3), 1738–1748.
- Bebout, G. E., & Penniston-Dorland, S. C. (2016). Fluid and mass transfer at subduction interfaces—the field metamorphic record. *Lithos*, 240, 228–258.

Behr, W. M., & Bürgmann, R. (2021). What's down there? the structures, materials and environment of deep-seated slow slip and tremor. *Philosophical Transactions of the Royal Society A*, 379(2193), 20200218.

- Behr, W. M., Gerya, T. V., Cannizzaro, C., & Blass, R. (2021). Transient slow slip characteristics of frictional-viscous subduction megathrust shear zones. *AGU Advances*, 2(3), e2021AV000416.
 - Bernabé, Y., Mok, U., & Evans, B. (2003). Permeability-porosity relationships in rocks subjected to various evolution processes. *Pure and Applied Geophysics*, 160, 937–960.
 - Bhattacharya, P., & Viesca, R. C. (2019). Fluid-induced aseismic fault slip outpaces pore-fluid migration. *Science*, 364 (6439), 464–468.
 - Bilham, R. (1989). Surface slip subsequent to the 24 november 1987 superstition hills, california, earthquake monitored by digital creepmeters. Bulletin of the Seismological Society of America, 79(2), 424–450.
 - Brantut, N., & David, E. C. (2019). Influence of fluids on vp/vs ratio: increase or decrease? Geophysical Journal International, 216(3), 2037–2043.
 - Bürgmann, R. (2018). The geophysics, geology and mechanics of slow fault slip. Earth and Planetary Science Letters, 495, 112–134.
 - Canales, J. P., Carbotte, S. M., Nedimović, M., & Carton, H. (2017). Dry juan de fuca slab revealed by quantification of water entering cascadia subduction zone. *Nature Geoscience*, 10(11), 864–870.
 - Cappa, F., Guglielmi, Y., & De Barros, L. (2022). Transient evolution of permeability and friction in a slowly slipping fault activated by fluid pressurization. *Nature communications*, 13(1), 3039.
 - Cappa, F., Guglielmi, Y., Nussbaum, C., De Barros, L., & Birkholzer, J. (2022). Fluid migration in low-permeability faults driven by decoupling of fault slip and opening. *Nature Geoscience*, 15(9), 747–751.
 - Chen, J. (2023). The emergence of four types of slow slip cycles on dilatant, fluid saturated faults. *Journal of Geophysical Research: Solid Earth*, 128(2), e2022JB024382.
 - Chen, J., Niemeijer, A., & Spiers, C. J. (2017). Microphysically derived expressions for rate-and-state friction parameters, a, b, and dc. *Journal of Geophysical Research: Solid Earth*, 122(12), 9627–9657.
 - Condit, C., & French, M. (2022). Geologic evidence of lithostatic pore fluid pressures at the base of the subduction seismogenic zone. *Geophysical Research Letters*, 49(12), e2022GL098862.
 - Condit, C. B., Guevara, V. E., Delph, J. R., & French, M. E. (2020). Slab dehydration in warm subduction zones at depths of episodic slip and tremor. *Earth and Planetary Science Letters*, 552, 116601.
 - Cordell, D., Naif, S., Evans, R., Key, K., Constable, S., Shillington, D., & Bécel, A. (2023). Forearc seismogenesis in a weakly coupled subduction zone influenced by slab mantle fluids. *Nature Geoscience*, 16(9), 822–827.
 - Cruz-Atienza, V. M., Villafuerte, C., & Bhat, H. S. (2018). Rapid tremor migration and pore-pressure waves in subduction zones. *Nature communications*, 9(1), 2900.
 - Dal Zilio, L., & Gerya, T. (2022). Subduction earthquake cycles controlled by episodic fluid pressure cycling. *Lithos*, 426, 106800.
 - David, C., Wong, T.-f., Zhu, W., & Zhang, J. (1994). Laboratory measurement of compaction-induced permeability change in porous rocks: Implications for the generation and maintenance of pore pressure excess in the crust. *Pure and applied geophysics*, 143, 425–456.
- Den Hartog, S., Niemeijer, A., & Spiers, C. J. (2012). New constraints on megathrust slip stability under subduction zone p-t conditions. *Earth and Planetary* Science Letters, 353, 240–252.
 - Dieterich, J. H. (1979). Modeling of rock friction: 1. experimental results and consti-

tutive equations. Journal of Geophysical Research: Solid Earth, 84 (B5), 2161-1232

1231

1234

1235

1237

1238

1241

1243

1244

1247

1248

1249

1250

1253

1256

1259

1260

1261

1262

1265

1267

1268

1270

1271

1272

1273

1274

1275

1277

1278

1279

1280

1283

1284

- Dublanchet, P. (2019). Fluid driven shear cracks on a strengthening rate-and-state frictional fault. Journal of the Mechanics and Physics of Solids, 132, 103672.
- Dublanchet, P., & De Barros, L. (2021). Dual seismic migration velocities in seismic swarms. Geophysical Research Letters, 48(1), e2020GL090025.
- Farge, G., Jaupart, C., Frank, W. B., & Shapiro, N. M. (2023). Along-strike segmentation of seismic tremor and its relationship with the hydraulic structure of the subduction fault zone. Journal of Geophysical Research: Solid Earth, 128(12), e2023JB027584.
- Faulkner, D., Jackson, C., Lunn, R., Schlische, R., Shipton, Z., Wibberley, C., & Withjack, M. (2010). A review of recent developments concerning the structure, mechanics and fluid flow properties of fault zones. Journal of Structural Geology, 32(11), 1557-1575.
- Fisher, D., Smye, A., Marone, C., Van Keken, P., & Yamaguchi, A. (2019). Kinetic models for healing of the subduction interface based on observations of ancient accretionary complexes. Geochemistry, Geophysics, Geosystems, 20(7), 3431 - 3449.
- Gao, H., Schmidt, D. A., & Weldon, R. J. (2012). Scaling relationships of source parameters for slow slip events. Bulletin of the Seismological Society of America, 102(1), 352-360.
- Garagash, D. (2012). Seismic and aseismic slip pulses driven by thermal pressurization of pore fluid. Journal of Geophysical Research: Solid Earth, 117(B4).
- Ghosh, A., Vidale, J. E., Sweet, J. R., Creager, K. C., Wech, A. G., Houston, H., & Brodsky, E. E. (2010). Rapid, continuous streaking of tremor in cascadia. Geochemistry, Geophysics, Geosystems, 11(12).
- Giger, S. B., Tenthorey, E., Cox, S. F., & Fitz Gerald, J. D. (2007).Permeability evolution in quartz fault gouges under hydrothermal conditions. Journal of Geophysical Research: Solid Earth, 112(B7).
- Gosselin, J. M., Audet, P., Estève, C., McLellan, M., Mosher, S. G., & Schaeffer, (2020).Seismic evidence for megathrust fault-valve behavior during episodic tremor and slip. Science Advances, 6(4), easy 5174.
- Goswami, A., & Barbot, S. (2018). Slow-slip events in semi-brittle serpentinite fault zones. Scientific reports, 8(1), 6181.
- Guglielmi, Y., Cappa, F., Avouac, J.-P., Henry, P., & Elsworth, D. (2015).micity triggered by fluid injection—induced aseismic slip. Science, 348 (6240),1224-1226.
- Hacker, B. R., Peacock, S. M., Abers, G. A., & Holloway, S. D. (2003). Subduction factory 2. are intermediate-depth earthquakes in subducting slabs linked to metamorphic dehydration reactions? Journal of Geophysical Research: Solid Earth, 108(B1).
- Hawthorne, J. C., & Rubin, A. M. (2013).Laterally propagating slow slip events in a rate and state friction model with a velocity-weakening to velocity-Journal of Geophysical Research: Solid Earth, strengthening transition. 118(7), 3785–3808.
- Heimisson, E. R., Dunham, E. M., & Almquist, M. (2019). Poroelastic effects destabilize mildly rate-strengthening friction to generate stable slow slip pulses. Journal of the Mechanics and Physics of Solids, 130, 262–279.
- Heimisson, E. R., Liu, S., Lapusta, N., & Rudnicki, J. (2022). A spectral boundaryintegral method for faults and fractures in a poroelastic solid: Simulations of a rate-and-state fault with dilatancy, compaction, and fluid injection. Journal of Geophysical Research: Solid Earth, 127(9), e2022JB024185.
- Heimisson, E. R., Rudnicki, J., & Lapusta, N. (2021). Dilatancy and compaction of a rate-and-state fault in a poroelastic medium: Linearized stability analysis. Journal of Geophysical Research: Solid Earth, 126(8), e2021JB022071.

Hooker, J., & Fisher, D. (2021). How cementation and fluid flow influence slip behavior at the subduction interface. *Geology*, 49(9), 1074–1078.

- Hosono, H., Takemura, T., Asahina, D., & Otsubo, M. (2022). Estimation of paleopermeability around a seismogenic fault based on permeability tensor from observable geometric information of quartz veins. Earth, Planets and Space, 74(1), 141.
 - Hyndman, R. D., McCrory, P. A., Wech, A., Kao, H., & Ague, J. (2015). Cascadia subducting plate fluids channelled to fore-arc mantle corner: Ets and silica deposition. *Journal of Geophysical Research: Solid Earth*, 120(6), 4344–4358.
 - Ide, S. (2012). Variety and spatial heterogeneity of tectonic tremor worldwide. *Journal of Geophysical Research: Solid Earth*, 117(B3).
 - Im, K., Elsworth, D., & Wang, C. (2019). Cyclic permeability evolution during repose then reactivation of fractures and faults. *Journal of Geophysical Research:* Solid Earth, 124(5), 4492–4506.
 - Im, K., Saffer, D., Marone, C., & Avouac, J.-P. (2020). Slip-rate-dependent friction as a universal mechanism for slow slip events. *Nature Geoscience*, 13(10), 705–710.
 - Ingebritsen, S. E., & Manning, C. (2010). Permeability of the continental crust: dynamic variations inferred from seismicity and metamorphism. *Geofluids*, 10(1-2), 193–205.
 - Ishibashi, T., Elsworth, D., Fang, Y., Riviere, J., Madara, B., Asanuma, H., ... Marone, C. (2018). Friction-stability-permeability evolution of a fracture in granite. Water Resources Research, 54(12), 9901–9918.
 - Kaneki, S., & Noda, H. (2023). Steady-state effective normal stress in subduction zones based on hydraulic models and implications for shallow slow earthquakes. *Journal of Geophysical Research: Solid Earth*, 128(2), e2022JB025995.
 - Katayama, I., Terada, T., Okazaki, K., & Tanikawa, W. (2012). Episodic tremor and slow slip potentially linked to permeability contrasts at the moho. *Nature Geoscience*, 5(10), 731–734.
 - Kato, N. (2003). A possible model for large preseismic slip on a deeper extension of a seismic rupture plane. Earth and Planetary Science Letters, 216(1-2), 17–25.
 - Kawano, S., Katayama, I., & Okazaki, K. (2011). Permeability anisotropy of serpentinite and fluid pathways in a subduction zone. *Geology*, 39(10), 939–942.
 - Khoshmanesh, M., & Shirzaei, M. (2018). Episodic creep events on the san andreas fault caused by pore pressure variations. *Nature Geoscience*, 11(8), 610–614.
 - Kirkpatrick, J. D., Fagereng, Å., & Shelly, D. R. (2021). Geological constraints on the mechanisms of slow earthquakes. Nature Reviews Earth & Environment, 2(4), 285–301.
 - Kodaira, S., Iidaka, T., Kato, A., Park, J.-O., Iwasaki, T., & Kaneda, Y.

 High pore fluid pressure may cause silent slip in the nankai trough.

 304 (5675), 1295–1298.
- Lauer, R. M., & Saffer, D. M. (2015). The impact of splay faults on fluid flow, solute transport, and pore pressure distribution in subduction zones: A case study offshore the n icoya p eninsula, c osta r ica. Geochemistry, Geophysics, Geosystems, 16(4), 1089–1104.
 - Lavier, L. L., Tong, X., & Biemiller, J. (2021). The mechanics of creep, slow slip events, and earthquakes in mixed brittle-ductile fault zones. *Journal of Geophysical Research: Solid Earth*, 126(2), e2020JB020325.
 - Li, D., & Liu, Y. (2016). Spatiotemporal evolution of slow slip events in a nonplanar fault model for northern cascadia subduction zone. *Journal of Geophysical Research: Solid Earth*, 121(9), 6828–6845.
 - Linker, M., & Dieterich, J. H. (1992). Effects of variable normal stress on rock friction: Observations and constitutive equations. *Journal of Geophysical Re-*

search: Solid Earth, 97(B4), 4923–4940.

- Liu, Y., & Rice, J. R. (2007). Spontaneous and triggered aseismic deformation transients in a subduction fault model. *Journal of Geophysical Research: Solid Earth*, 112(B9).
- Liu, Y., & Rubin, A. M. (2010). Role of fault gouge dilatancy on assismic deformation transients. *Journal of Geophysical Research: Solid Earth*, 115(B10).
- Lockner, D., Naka, H., Tanaka, H., Ito, H., & Ikeda, R. (2000). Permeability and strength of core samples from the nojima fault of the 1995 kobe earthquake. In *Proceedings of the international workshop on the nojima fault core and borehole data analysis* (Vol. 129, pp. 147–152).
- Lockner, D. A., Tanaka, H., Ito, H., Ikeda, R., Omura, K., & Naka, H. (2009). Geometry of the nojima fault at nojima-hirabayashi, japan–i. a simple damage structure inferred from borehole core permeability. *Pure and Applied Geophysics*, 166, 1649–1667.
- Luo, Y., & Liu, Z. (2021). Fault zone heterogeneities explain depth-dependent pattern and evolution of slow earthquakes in cascadia. *Nature Communications*, 12(1), 1959.
- Marguin, V., & Simpson, G. (2023). Influence of fluids on earthquakes based on numerical modeling. *Journal of Geophysical Research: Solid Earth*, 128(2), e2022JB025132.
- Marone, C. (1998). Laboratory-derived friction laws and their application to seismic faulting. Annual Review of Earth and Planetary Sciences, 26(1), 643–696.
- Materna, K., Bürgmann, R., Lindsay, D., Bilham, R., Herring, T., Crowell, B., & Szeliga, W. (2024). Shallow slow slip events in the imperial valley with along-strike propagation. *Geophysical Research Letters*, 51(12), e2023GL108089.
- Matsuzawa, T., Shibazaki, B., Obara, K., & Hirose, H. (2013). Comprehensive model of short-and long-term slow slip events in the shikoku region of japan, incorporating a realistic plate configuration. Geophysical Research Letters, 40(19), 5125–5130.
- Mattsson, K. (2012). Summation by parts operators for finite difference approximations of second-derivatives with variable coefficients. *Journal of Scientific Computing*, 51(3), 650–682.
- Mavko, G., Mukerji, T., & Dvorkin, J. (2020). The rock physics handbook. Cambridge university press.
- McLellan, M., Audet, P., Rosas, J. C., & Currie, C. (2022). Margin-wide variations in slab dehydration in cascadia and their relationship to slow slip. *Lithos*, 434, 106912.
- Mei, C., & Wang, L. (2024). Velocity dependence of rate-and-state friction in granular fault gouge and implications for slow-slip events. *Journal of Geophysical Research: Solid Earth*, 129(7), e2024JB029393.
- Menant, A., Angiboust, S., & Gerya, T. (2019). Stress-driven fluid flow controls long-term megathrust strength and deep accretionary dynamics. Scientific reports, 9(1), 9714.
- Mitchell, T., & Faulkner, D. (2012). Towards quantifying the matrix permeability of fault damage zones in low porosity rocks. *Earth and Planetary Science Letters*, 339, 24–31.
- Morishige, M., & van Keken, P. E. (2017). Along-arc variation in short-term slow slip events caused by 3-d fluid migration in subduction zones. *Journal of Geophysical Research: Solid Earth*, 122(2), 1434–1448.
- Morrow, C. A., Moore, D. E., & Lockner, D. (2001). Permeability reduction in granite under hydrothermal conditions. *Journal of Geophysical Research: Solid Earth*, 106 (B12), 30551–30560.
- Muñoz-Montecinos, J., & Behr, W. M. (2023). Transient permeability of a deepseated subduction interface shear zone. *Geophysical Research Letters*, 50(20), e2023GL104244.

Naif, S., Key, K., Constable, S., & Evans, R. L. (2016). Porosity and fluid budget of a water-rich megathrust revealed with electromagnetic data at the m iddle a merica t rench. Geochemistry, Geophysics, Geosystems, 17(11), 4495–4516.

- Nakano, M., Hori, T., Araki, E., Kodaira, S., & Ide, S. (2018). Shallow very-low-frequency earthquakes accompany slow slip events in the nankai subduction zone. *Nature communications*, 9(1), 984.
 - Nakatani, M., & Scholz, C. H. (2006). Intrinsic and apparent short-time limits for fault healing: Theory, observations, and implications for velocity-dependent friction. *Journal of Geophysical Research: Solid Earth*, 111(B12).
 - Nie, S., & Barbot, S. (2021). Seismogenic and tremorgenic slow slip near the stability transition of frictional sliding. *Earth and Planetary Science Letters*, 569, 117037.
 - Nishikawa, T., Matsuzawa, T., Ohta, K., Uchida, N., Nishimura, T., & Ide, S. (2019). The slow earthquake spectrum in the japan trench illuminated by the s-net seafloor observatories. *Science*, 365(6455), 808–813.
 - Nishiyama, N., Sumino, H., & Ujiie, K. (2020). Fluid overpressure in subduction plate boundary caused by mantle-derived fluids. Earth and Planetary Science Letters, 538, 116199.
 - Nuyen, C. P., & Schmidt, D. A. (2021). Filling the gap in cascadia: The emergence of low-amplitude long-term slow slip. *Geochemistry, Geophysics, Geosystems*, 22(3), e2020GC009477.
 - Obara, K. (2010). Phenomenology of deep slow earthquake family in southwest japan: Spatiotemporal characteristics and segmentation. *Journal of Geophysical Research: Solid Earth*, 115(B8).
 - Obara, K., Matsuzawa, T., Tanaka, S., & Maeda, T. (2012). Depth-dependent mode of tremor migration beneath kii peninsula, nankai subduction zone. *Geophysical Research Letters*, 39(10).
 - Okuda, H., Kitamura, M., Takahashi, M., & Yamaguchi, A. (2023). Frictional properties of the décollement in the shallow nankai trough: constraints from friction experiments simulating in-situ conditions and implications for the seismogenic zone. Earth and Planetary Science Letters, 621, 118357.
 - Okuda, H., Niemeijer, A. R., Takahashi, M., Yamaguchi, A., & Spiers, C. J. (2023). Hydrothermal friction experiments on simulated basaltic fault gouge and implications for megathrust earthquakes. *Journal of Geophysical Research: Solid Earth*, 128(1), e2022JB025072.
 - Otsubo, M., Hardebeck, J. L., Miyakawa, A., Yamaguchi, A., & Kimura, G. (2020). Localized fluid discharge by tensile cracking during the post-seismic period in subduction zones. *Scientific Reports*, 10(1), 12281.
 - Ozawa, S. (2024a, March). Scripts used to produce the results presented in ozawa et al. (2024) [software]. Stanford Digital Repository. Retrieved from https://doi.org/10.25740/bq498cn4340 doi: doi.org/10.25740/bq498cn4340
 - Ozawa, S. (2024b, March). sozawa94/hbi: Faultvalve2d [software]. Zenodo. Retrieved from https://doi.org/10.5281/zenodo.10855266 doi: 10.5281/zenodo.10855266
- Ozawa, S., Ida, A., Hoshino, T., & Ando, R. (2023). Large-scale earthquake sequence simulations on 3-d non-planar faults using the boundary element method accelerated by lattice h-matrices. *Geophysical Journal International*, 232(3), 1471–1481.
- Ozawa, S. W., Hatano, T., & Kame, N. (2019). Longer migration and spontaneous decay of aseismic slip pulse caused by fault roughness. *Geophysical Research Letters*, 46(2), 636–643.
- Peacock, S. M. (1990). Fluid processes in subduction zones. *Science*, 248 (4953), 329–337.
- Peacock, S. M., Christensen, N. I., Bostock, M. G., & Audet, P. (2011). High pore pressures and porosity at 35 km depth in the cascadia subduction zone. *Geol-*

ogy, 39(5), 471-474.

1451

1454

1455

1456

1457

1459

1460

1461

1462

1464

1465

1466

1467

1469

1470

1471

1472

1474

1475

1476

1479

1480

1481

1483

1484

1485

1486

1488

1489

1490

1493

1494

1496

1499

1500

1501

1502

- Perez-Silva, A., Kaneko, Y., Savage, M., Wallace, L., & Warren-Smith, E. (2023). Characteristics of slow slip events explained by rate-strengthening faults subject to periodic pore fluid pressure changes. *Journal of Geophysical Research:* Solid Earth, 128(6), e2022JB026332.
- Perfettini, H., & Molinari, A. (2023). The interaction between frictional slip and viscous fault root produces slow slip events. *Journal of Geophysical Research:* Solid Earth, 128(3), e2022JB024645.
- Petrini, C., Gerya, T., Yarushina, V., van Dinther, Y., Connolly, J., & Madonna, C. (2020). Seismo-hydro-mechanical modelling of the seismic cycle: Methodology and implications for subduction zone seismicity. *Tectonophysics*, 791, 228504.
- Press, W., Tenkolsky, W., et al. (2002). Numerical recipes in fortran 90: The art of parralel scientific compputing. University Press Cambrige.
- Rice, J. R. (1992). Fault stress states, pore pressure distributions, and the weakness of the san andreas fault. In *International geophysics* (Vol. 51, pp. 475–503). Elsevier.
- Rice, J. R. (1993). Spatio-temporal complexity of slip on a fault. *Journal of Geo*physical Research: Solid Earth, 98 (B6), 9885–9907.
- Rice, J. R. (2006). Heating and weakening of faults during earthquake slip. *Journal of Geophysical Research: Solid Earth*, 111(B5).
- Rice, J. R., Lapusta, N., & Ranjith, K. (2001). Rate and state dependent friction and the stability of sliding between elastically deformable solids. *Journal of the Mechanics and Physics of Solids*, 49(9), 1865–1898.
- Rogers, G., & Dragert, H. (2003). Episodic tremor and slip on the cascadia subduction zone: The chatter of silent slip. Science, 300(5627), 1942-1943.
- Romanet, P., Bhat, H. S., Jolivet, R., & Madariaga, R. (2018). Fast and slow slip events emerge due to fault geometrical complexity. *Geophysical Research Letters*, 45(10), 4809–4819.
- Rubin, A. M. (2008). Episodic slow slip events and rate-and-state friction. *Journal of Geophysical Research: Solid Earth*, 113(B11).
- Rubin, A. M. (2011). Designer friction laws for bimodal slow slip propagation speeds. *Geochemistry, Geophysics, Geosystems*, 12(4).
- Ruina, A. (1983). Slip instability and state variable friction laws. *Journal of Geo*physical Research: Solid Earth, 88 (B12), 10359–10370.
- Sáez, A., Lecampion, B., Bhattacharya, P., & Viesca, R. C. (2022). Three-dimensional fluid-driven stable frictional ruptures. Journal of the Mechanics and Physics of Solids, 160, 104754.
- Saffer, D. M. (2012). The permeability of active subduction plate boundary faults. Crustal Permeability, 207–227.
- Saffer, D. M., & Tobin, H. J. (2011). Hydrogeology and mechanics of subduction zone forearcs: Fluid flow and pore pressure. *Annual Review of Earth and Planetary Sciences*, 39(1), 157–186.
- Saishu, H., Okamoto, A., & Otsubo, M. (2017). Silica precipitation potentially controls earthquake recurrence in seismogenic zones. *Scientific reports*, 7(1), 13337.
- Sakamoto, R., & Tanaka, Y. (2022). Frictional and hydraulic properties of plate interfaces constrained by a tidal response model considering dilatancy/compaction. *Journal of Geophysical Research: Solid Earth*, 127(8), e2022JB024112.
- Sawai, M., Niemeijer, A. R., Plümper, O., Hirose, T., & Spiers, C. J. (2016). Nucleation of frictional instability caused by fluid pressurization in subducted blueschist. *Geophysical Research Letters*, 43(6), 2543–2551.
- Scholz, C. H. (1998). Earthquakes and friction laws. *Nature*, 391 (6662), 37–42.
 - Segall, P. (2010). Earthquake and volcano deformation. Princeton University Press.

Segall, P., & Rice, J. R. (2006). Does shear heating of pore fluid contribute to earth-quake nucleation? *Journal of Geophysical Research: Solid Earth*, 111(B9).

- Segall, P., Rubin, A. M., Bradley, A. M., & Rice, J. R. (2010). Dilatant strengthening as a mechanism for slow slip events. *Journal of Geophysical Research: Solid Earth*, 115 (B12).
- Shibazaki, B., & Iio, Y. (2003). On the physical mechanism of silent slip events along the deeper part of the seismogenic zone. *Geophysical Research Letters*, 30(9).
- Shimamoto, T. (1986). Transition between frictional slip and ductile flow for halite shear zones at room temperature. *Science*, 231(4739), 711–714.
- Shreedharan, S., Ikari, M., Wood, C., Saffer, D., Wallace, L., & Marone, C. (2022) Frictional and lithological controls on shallow slow slip at the northern hikurangi margin. *Geochemistry, Geophysics, Geosystems*, 23(2), e2021GC010107.
- Sibson, R. (1992). Implications of fault-valve behaviour for rupture nucleation and recurrence. *Tectonophysics*, 211(1-4), 283–293.
- Skarbek, R. M., & Rempel, A. W. (2016). Dehydration-induced porosity waves and episodic tremor and slip. *Geochemistry, Geophysics, Geosystems*, 17(2), 442–469.
- Skarbek, R. M., Rempel, A. W., & Schmidt, D. A. (2012). Geologic heterogeneity can produce aseismic slip transients. *Geophysical Research Letters*, 39(21).
- Takagi, R., Uchida, N., & Obara, K. (2019). Along-strike variation and migration of long-term slow slip events in the western nankai subduction zone, japan. *Journal of Geophysical Research: Solid Earth*, 124(4), 3853–3880.
- Talwani, P., Chen, L., & Gahalaut, K. (2007). Seismogenic permeability, ks. *Journal of Geophysical Research: Solid Earth*, 112(B7).
- Tanaka, Y., Suzuki, T., Imanishi, Y., Okubo, S., Zhang, X., Ando, M., ... others (2018). Temporal gravity anomalies observed in the tokai area and a possible relationship with slow slips. *Earth, Planets and Space*, 70, 1–8.
- Tarling, M. S., Smith, S. A., & Scott, J. M. (2019). Fluid overpressure from chemical reactions in serpentinite within the source region of deep episodic tremor. Nature Geoscience, 12(12), 1034–1042.
- Tenthorey, E., & Gerald, J. D. F. (2006). Feedbacks between deformation, hydrothermal reaction and permeability evolution in the crust: Experimental insights. *Earth and Planetary Science Letters*, 247(1-2), 117–129.
- Thomas, A., Bürgmann, R., Shelly, D. R., Beeler, N. M., & Rudolph, M. (2012). Tidal triggering of low frequency earthquakes near parkfield, california: Implications for fault mechanics within the brittle-ductile transition. *Journal of Geophysical Research: Solid Earth*, 117(B5).
- Tse, S. T., & Rice, J. R. (1986). Crustal earthquake instability in relation to the depth variation of frictional slip properties. *Journal of Geophysical Research:* Solid Earth, 91(B9), 9452–9472.
- Ujiie, K., Saishu, H., Fagereng, Å., Nishiyama, N., Otsubo, M., Masuyama, H., & Kagi, H. (2018). An explanation of episodic tremor and slow slip constrained by crack-seal veins and viscous shear in subduction mélange. *Geophysical Research Letters*, 45(11), 5371–5379.
- Van Keken, P. E., Hacker, B. R., Syracuse, E. M., & Abers, G. A. (2011). Subduction factory: 4. depth-dependent flux of h2o from subducting slabs worldwide. *Journal of Geophysical Research: Solid Earth*, 116(B1).
- Warren-Smith, E., Fry, B., Wallace, L., Chon, E., Henrys, S., Sheehan, A., ... Lebedev, S. (2019). Episodic stress and fluid pressure cycling in subducting oceanic crust during slow slip. *Nature Geoscience*, 12(6), 475–481.
- Wech, A. G., & Creager, K. C. (2011). A continuum of stress, strength and slip in the cascadia subduction zone. *Nature Geoscience*, 4(9), 624–628.
- Wei, M., Kaneko, Y., Liu, Y., & McGuire, J. J. (2013). Episodic fault creep events in california controlled by shallow frictional heterogeneity. *Nature geoscience*,

6(7), 566–570.

- Wibberley, C. A., & Shimamoto, T. (2003). Internal structure and permeability of major strike-slip fault zones: the median tectonic line in mie prefecture, southwest japan. *Journal of Structural Geology*, 25(1), 59–78.
- Williams, R. T., & Fagereng, Å. (2022). The role of quartz cementation in the seismic cycle: A critical review. *Reviews of Geophysics*, 60(1), e2021RG000768.
- Wilson, C. R., Spiegelman, M., van Keken, P. E., & Hacker, B. R. (2014). Fluid flow in subduction zones: The role of solid rheology and compaction pressure. *Earth and Planetary Science Letters*, 401, 261–274.
- Xue, L., Li, H.-B., Brodsky, E. E., Xu, Z.-Q., Kano, Y., Wang, H., ... others (2013). Continuous permeability measurements record healing inside the wenchuan earthquake fault zone. *Science*, 340 (6140), 1555–1559.
- Yamashita, T. (2013). Generation of slow slip coupled with tremor due to fluid flow along a fault. *Geophysical Journal International*, 193(1), 375–393.
- Yang, Y., & Dunham, E. M. (2021). Effect of porosity and permeability evolution on injection-induced aseismic slip. *Journal of Geophysical Research: Solid Earth*, 126(7), e2020JB021258.
- Yang, Y., & Dunham, E. M. (2023). Influence of creep compaction and dilatancy on earthquake sequences and slow slip. Journal of Geophysical Research: Solid Earth, 128(4), e2022JB025969.
- Ye, Z., & Ghassemi, A. (2018). Injection-induced shear slip and permeability enhancement in granite fractures. *Journal of Geophysical Research: Solid Earth*, 123(10), 9009–9032.
- Yehya, A., & Rice, J. R. (2020). Influence of fluid-assisted healing on fault permeability structure. *Journal of Geophysical Research: Solid Earth*, 125(10), e2020JB020553.
- Zhu, W., Allison, K. L., Dunham, E. M., & Yang, Y. (2020). Fault valving and pore pressure evolution in simulations of earthquake sequences and aseismic slip. *Nature communications*, 11(1), 4833.
- Zhu, W., & Wong, T.-f. (1997). The transition from brittle faulting to cataclastic flow: Permeability evolution. *Journal of Geophysical Research: Solid Earth*, 102(B2), 3027–3041.